



HAL
open science

Structure–Property Relationships in Photoluminescent Bismuth Halide Organic Hybrid Materials

R. Lee Ayscue, Valérie Vallet, Jeffery A. Bertke, Florent Réal, Karah E. Knope

► **To cite this version:**

R. Lee Ayscue, Valérie Vallet, Jeffery A. Bertke, Florent Réal, Karah E. Knope. Structure–Property Relationships in Photoluminescent Bismuth Halide Organic Hybrid Materials. *Inorganic Chemistry*, 2021, 60 (13), pp.9727–9744. 10.1021/acs.inorgchem.1c01025 . hal-03262995

HAL Id: hal-03262995

<https://hal.science/hal-03262995>

Submitted on 25 Aug 2021

HAL is a multi-disciplinary open access archive for the deposit and dissemination of scientific research documents, whether they are published or not. The documents may come from teaching and research institutions in France or abroad, or from public or private research centers.

L'archive ouverte pluridisciplinaire **HAL**, est destinée au dépôt et à la diffusion de documents scientifiques de niveau recherche, publiés ou non, émanant des établissements d'enseignement et de recherche français ou étrangers, des laboratoires publics ou privés.

Structure-Property Relationships in Photoluminescent Bismuth Halide Organic Hybrid Materials

R. Lee Ayscue III,† Valérie Vallet,‡ Jeffery A. Bertke,† Florent Réal,‡, and Karah E. Knope†**

† Department of Chemistry, Georgetown University, 37th and O Streets, NW, Washington, D.C. 20057, USA

‡ Univ. Lille, CNRS, UMR 8523–PhLAM–Physique des Lasers Atomes et Molécules, 59000 Lille, France

KEYWORDS

Bismuth, Halide, Photoluminescence, Electronic Structure Calculations, Doping, Color Tuning

ABSTRACT

Seven novel bismuth(III)-halide phases, $[\text{Bi}_2\text{Cl}_6(\text{terpy})_2](\text{H}_2\text{O})_{0.5}$ (**1**), $\text{Bi}_2\text{Cl}_4(\text{terpy})_2(\text{k}_2\text{-TC})_2$ (**2**), $\text{BiCl}(\text{terpy})(\text{k}_2\text{-TC})_2$ (**3A-Cl**), $\text{BiBr}(\text{terpy})(\text{k}_2\text{-TC})_2$ (**3A-Br**), $\text{BiCl}(\text{terpy})(\text{k}_2\text{-TC})_2$ (**3B-Cl**), $[\text{BiCl}(\text{terpy})(\text{k}_2\text{-TC})_2][\text{Bi}(\text{terpy})(\text{k}_2\text{-TC})_3]\cdot 0.55(\text{TCA})$ (**4**), $[\text{BiBr}_3(\text{terpy})(\text{MeOH})]$ (**5**), and $[\text{BiBr}_2(\text{terpy})(\text{k}_2\text{-TC})][\text{BiBr}_{1.16}(\text{terpy})(\text{k}_2\text{-TC})_{1.84}]$ (**6**), were prepared under mild synthetic conditions from methanolic/aqueous solutions containing BiX_3 ($X = \text{Cl}, \text{Br}$) and 2,2',6',2''-terpyridine (terpy) and/or 2-thiophene monocarboxylic acid (TCA). A heterometallic series, **3A-Bi_{1-x}Eu_xCl**, with the general formula $\text{Bi}_{1-x}\text{Eu}_x\text{Cl}(\text{terpy})(\text{k}_2\text{-TC})_2$ ($x = 0.001, 0.005, 0.01, 0.05$) was

also prepared through trace Eu doping of the **3A-CI** phase. The structures were determined through single crystal X-ray diffraction and are built from a range of molecular units including monomeric and dimeric complexes. The solid-state photoluminescent properties of the compounds were examined through steady-state and time resolved methods. While the homometallic phases exhibited broad green to yellow emission, the heterometallic phases displayed yellow, orange, and red emission that can be attributed to the simultaneous ligand/Bi-halide and Eu centered emissions. Photoluminescent color tuning was achieved by controlling the relative intensities of these concurrent emissions through compositional modifications including the Eu doping percentage. Notably, all emissive homo- and heterometallic phases exhibited rare visible excitation pathways that based on theoretical quantum mechanical calculations, are attributed to halide-metal to ligand charge transfer (XMLCT). Through a combined experimental and computational approach, fundamental insight into the structure property relationships within these Bi halide organic hybrid materials is provided.

INTRODUCTION

Ongoing demand for tailorable photoluminescent materials and novel design strategies have been the focus of many research efforts across the gamut of inorganic (e.g., perovskite photovoltaics/lighting phosphors/nanomaterials),¹⁻⁴ organic (e.g., luminescent dyes),⁵⁻⁶ and hybrid (e.g., sensors/aggregation induced emitters/Ln emissive materials)⁷⁻¹⁰ materials research. At the core of all these studies are the development of fundamental knowledge and subsequent utilization of underlying structure-property relationships to obtain optimized, tailored, and controlled materials properties including compositional control of emission,¹¹⁻¹⁴ radical stabilizing molecular functionalities,¹⁵⁻¹⁶ and/or synergistic metal ligand energy relationships.¹⁷⁻¹⁹ In recent years,

bismuth halide based photoactive materials have gained significant attention in photovoltaics, photocatalysts, and photoluminescent materials.²⁰⁻²² Focusing on the latter, Bi halide organic systems have exhibited a range of interesting luminescent behaviors including reversible mechanochromism, Ln sensitization, and white light emission as observed in halobismuthates, layered perovskites, and coordination polymers.²³⁻²⁵

Within these materials, luminescence has been attributed to a number of pathways including metal centered emission originating from the closed shell $6s^2 \text{Bi}^{3+}$ metal center and/or lanthanide ions doped into the bismuth framework or otherwise ligand based emission.²⁶⁻²⁹ Furthermore, charge transfer mechanisms including MLCT, LMCT, and IVCT offer an even broader range of transitions that may underpin the observed luminescent behavior.³⁰⁻³² Luminescent homometallic Bi-based materials often exhibit broad emissive features that have relatively ambiguous origins upon qualitative inspection. Although certain photophysical features including lifetimes, Stokes shift, and peak position can provide insight into the assignment of the broad emissions, quantum mechanical molecular orbital calculations have proved quite valuable in discerning the structural origins of luminescence in bismuth-based materials.^{30, 33} As such, a combined experimental and computation approach aimed at elucidating the photophysical behavior of bismuth-based compounds built from discrete molecular units was pursued in this work.

While Bi coordination polymers and metal-organic frameworks have exhibited interesting luminescent behavior, our goal in targeting discrete molecular systems was to identify the intra- and intermolecular interactions (e.g., metal-ligand coordination, halide identity, metal complex nuclearity, and supramolecular packing interactions) that facilitate the observed luminescent behavior in homo- and heterometallic bismuth-halide-organic compounds. From a computational perspective, such complexes may also provide a more manageable starting point for understanding

the effects of intra- and intermolecular structural motifs on photophysical properties than extended network materials. Thus, 2,2',6',2''-terpyridine (terpy) and 2-thiophenemonocarboxylate (TC) were employed to restrict the complex dimensionality through terminal or 'capping' coordination. Furthermore, both chloride and bromide phases were targeted in order to examine the effects of halide identity on bismuth coordination, as well as reveal any discernable trends in photoluminescent behavior.

In this work seven novel homometallic Bi-halide-organic phases built from monomeric, dimeric, and/or cocrystallized molecular units are presented. The solid-state photoluminescent properties of the compounds were examined through steady-state and time resolved methods and five of the homometallic phases exhibited broad green to yellow emission with excitation profiles that extend well into the visible region. Lanthanide doping into the bismuth phases was additionally pursued, and an Eu doped heterometallic series revealed simultaneous broad band emission, as seen in the homometallic analog, as well as sensitized Eu emission. Interestingly, compositional based photoluminescent color tuning (PLCT) was achieved upon adjustment of the Eu doping percentage. Moreover, the aforementioned visible excitation pathway was retained in the heterometallic system. In an effort to understand the origin of luminescence in these phases, structure-property relationships were investigated. The structures were determined through single crystal X-ray diffraction (SCXRD) and quantum mechanical calculations using structural models obtained from the experimentally determined single-crystal structures were performed to better understand the origins of the observed excitation and emissive pathways. The computational studies showed that the frontier orbitals responsible for the visible excitation originate from intramolecular halide-metal to ligand charge transfer (XMLCT), for which strong orbital mixing within the BiX sub-unit is observed in the principal highest occupied molecular orbital (HOMO)

energetic state. Comparison of the experimental excitation spectra with the calculated absorption transitions further revealed that both ligand orientation and the number of halide substituents bound within the Bi anchored complex influence the degree to which the excitation bands extend into the visible region. This work provides fundamental insight into structure-property relationships that govern photoluminescence in Bi halide organic hybrid compounds and further demonstrates their utility as a promising class of photoactive materials.

EXPERIMENTAL SECTION

Materials. BiCl₃ 99.9%, BiBr₃ 99% (Alfa Aesar); EuCl₃•6H₂O 99.9% (Strem Chemicals); 2-thiophenecarboxylic acid 99%, 2,2':6',2''-terpyridine 96%, KCl 99+% (Acros Organic); poly(methyl methacrylate) (PMMA) MW=12,000, Methanol ACS grade (Sigma-Aldrich); KNO₃ 99%, KOH flake technical grade, and HNO₃ 68-70 wt% (Fisher Chemical) were used as received. Nanopure water (≤0.05 μS; Millipore, USA) was used in all denoted preparations.

General Synthetic Procedure.

In a typical synthesis, the bismuth halide salt (BiCl₃ or BiBr₃), 2,2',6',2''-terpyridine (terpy), and 2-thiophene monocarboxylic acid (TCA) were combined in a methanolic and/or aqueous solution. Slight variations in reaction pH (2-5), time (0.1-48 hours), temperature (20-50 °C), and reagent stoichiometry as described in the Supporting Information led to the isolation of seven unique Bi-halide-organic phases. Additionally, a lanthanide doped heterometallic series, **3A-Bi_{1-x}Eu_xCl** (x = 0.001, 0.005, 0.01, 0.05), was produced upon partial substitution of BiCl₃ by EuCl₃ starting materials at 0.1, 0.5, 1, and 5% Eu. All other synthetic conditions were maintained as described for the homometallic analog, **3A-Cl**. Note that while previous work has shown that lanthanides often incorporate into Bi host materials at much lower doping percentages than those used in the synthesis,^{52,56} due to phase impurities for several of the doped samples, the reported Eu doping

percentages correspond to the amount of Eu^{3+} relative to Bi^{3+} used in the synthesis. An increase in Eu doping percentage with increased synthetic loading is consistent with an increase in Eu emission across the doped samples from 0.1-1% Eu doping.

While compounds **1**, **2**, **3A-Br**, and **4-6** could be obtained as phase pure products, efforts to remove trace impurities, KCl and KNO_3 , from the syntheses of **3A-Cl**, **3B-Cl**, and the **3A-Bi_xEu_xCl** ($x = 0.001, 0.005, 0.01, 0.05$) series were unsuccessful. In fact, efforts to prevent and/or remove the impurities via reagent substitutions, washing methods, and separation techniques led to impurity retention, phase separation, and/or degradation of the desired product. The poor solubility of Bi halide salts in water or common organic solvents serves as a principal challenge. However, this limited solubility also likely serves as a synthetic driving force for the rich structural diversity seen within Bi hybrid materials. Additions of nitric acid afforded full dissolution of the BiCl_3 starting material and thwarted bismuth oxychloride formation. However, additions of HNO_3 resulted in coprecipitation of potassium nitrate (KNO_3) and potassium chloride (KCl) salts. Attempts to fully remove or avoid KCl and KNO_3 byproduct resulted in the unwanted phase conversion of the desired products. Further synthetic details for each compound along with elemental analysis for the phase pure products are provided in the Supporting Information; a discussion of the key synthetic parameters that led to the isolation of each phase is provided below.

Structure Determination. Single crystals were isolated from the bulk reaction product and mounted in Paratone-N oil on MiTeGen micro-mounts. Single crystal X-ray diffraction data for **1**, **2**, **3A-Cl**, **3A-Br**, **3B-Cl**, **4-6**, were collected at 100(2) K on a Bruker D8 Quest diffractometer equipped with an $\text{I}\mu\text{S}$ X-ray source (Mo- $\text{K}\alpha$ radiation; $\lambda=0.71073 \text{ \AA}$) and a Photon 100 CMOS detector. Data were collected and integrated using the APEX3/SHELX-2017 suite of

crystallographic software.³⁴ Absorption corrections were applied using a multi-scan technique in SADABS. The structures were solved using intrinsic phasing methods via SHELXT and refined in SHELXLE utilizing full-matrix least-squares of F^2 .³⁵⁻³⁶ During the refinements, all carbon bound hydrogen atoms were placed in calculated positions, while H atoms on oxygen atoms were located in the difference map. The latter H atoms were restrained with distance (DFIX) and angle (DANG) restraints of 0.86(1) and 1.43(1), respectively, and were assigned as 1.5 times the U_{eq} of the carrier atom. Positional disorder of several of the thiophene rings was observed and hence the organic unit was refined over two orientations. The like S-C and C-C distances within the rings were restrained to be similar (SADI). When appropriate, rigid-bond restraints (RIGU) were imposed on displacement parameters for disordered sites, and similar displacement amplitudes (SIMU) were imposed on disordered sites overlapping by less than the sum of the Van der Waals radii. Atoms that exhibited shifting displacement parameters were treated with mild isotropic restraints (ISOR). Intermolecular interactions, bond distances, and torsion angles were assessed using the PLATON software suite.³⁷

Crystallographic refinement details for the homometallic phases are provided in Table 1. Further structure refinement details and thermal ellipsoid plots (Figures S1-S8) are provided as Supporting Information. CIF data are also available as ESI and were submitted to the Cambridge Structural Data Centre (CCDC), www.ccdc.cam.ac.uk/by, and may be obtained by referencing codes 2063326-2063333.

Table 1: Crystallographic refinement details for **1, 2, 3A-Cl, 3A-Br, 3B-Cl, 4-6.**

	1	2	3A-Cl	3A-Br
Chemical Formula	Bi ₂ Cl ₆ ON ₆ C ₃₀ H ₂₄	Bi ₂ Cl ₄ S ₂ O ₄ N ₆ C ₄₀ H ₂₈	BiClS ₂ O ₄ N ₃ C ₂₅ H ₁₇	BiBrS ₂ O ₄ N ₃ C ₂₅ H ₁₇
MW (g mol ⁻¹)	1115.21	1280.56	731.96	776.42
Crystal System	Triclinic	Triclinic	Triclinic	Triclinic
Space Group	P-1	P-1	P-1	P-1
<i>a</i> (Å)	8.538(13)	9.2018(5)	11.1563(5)	11.2043(4)
<i>b</i> (Å)	10.891(19)	11.2953(6)	11.5682(5)	11.6167(4)
<i>c</i> (Å)	18.250(30)	12.0209(6)	11.5730(5)	11.6199(4)
α (°)	92.850(40)	97.792(3)	111.3733(13)	111.0740(14)
β (°)	100.690(30)	110.551(2)	106.2909(14)	106.4303(14)
γ (°)	95.330(30)	113.071(2)	106.1535(14)	106.4768(14)
<i>V</i> (Å ³)	1656(5)	1020.80(9)	1208.06(9)	1221.75(8)
<i>Z</i>	2	1	2	2
<i>T</i> (K)	100(2)	100(2)	100(2)	100(2)
λ Mo K α (Å)	0.71073	0.71073	0.71073	0.71073
<i>D</i> _{calc} (g cm ⁻³)	2.236	2.083	2.012	2.111
μ (mm ⁻¹)	11.132	9.022	7.620	9.061
<i>R</i> _{int}	0.0478	0.0534	0.0287	0.0313
<i>R</i> ₁ [<i>I</i> > 2 σ (<i>I</i>)]	0.0276	0.0342	0.0384	0.0394
<i>wR</i> ₂ [<i>I</i> > 2 σ (<i>I</i>)]	0.0420	0.0484	0.0757	0.1025
CCDC Number	2063326	2063327	2063328	2063329
	3B-Cl	4	5	6
Chemical Formula	BiClS ₂ O ₄ N ₃ C ₂₅ H ₁₇	Bi ₄ Cl ₂ S ₁₁ O ₂₂ N ₁₂ C ₁₁₅ H ₇₈	Bi ₂ Br ₆ O ₂ N ₆ C ₃₂ H ₃₀	Bi ₂ Br _{3.16} S _{2.84} O _{5.68} N ₆ C _{44.21} H _{30.52}
MW (g mol ⁻¹)	731.96	3239.37	1428.04	1498.22
Crystal System	Triclinic	Triclinic	Triclinic	Triclinic
Space Group	P-1	P-1	P-1	P-1
<i>a</i> (Å)	9.5873(5)	11.0433(7)	9.0492(7)	10.8619(7)
<i>b</i> (Å)	10.5258(6)	16.8045(11)	10.6363(9)	13.6808(8)
<i>c</i> (Å)	14.0462(8)	17.7423(11)	20.3345(17)	15.7444(10)
α (°)	70.1070(10)	115.951(2)	89.026(3)	79.546(2)
β (°)	76.8070(10)	98.869(2)	78.240(3)	79.021(2)
γ (°)	66.1520(10)	102.008(2)	88.845(2)	78.962(2)
<i>V</i> (Å ³)	1212.29(12)	2781.0(3)	1915.6(3)	2228.6(2)
<i>Z</i>	2	1	4	2
<i>T</i> (K)	100(2)	100(2)	100(2)	100(2)
λ Mo K α (Å)	0.71073	0.71073	0.71073	0.71073
<i>D</i> _{calc} (g cm ⁻³)	2.005	1.934	2.476	2.233
μ (mm ⁻¹)	7.594	6.643	15.470	10.907
<i>R</i> _{int}	0.0206	0.0448	0.0466	0.0533
<i>R</i> ₁ [<i>I</i> > 2 σ (<i>I</i>)]	0.0102	0.0337	0.0219	0.0238
<i>wR</i> ₂ [<i>I</i> > 2 σ (<i>I</i>)]	0.0262	0.0721	0.0367	0.0407
CCDC Number	2063330	2063331	2063332	2063333

Bulk Sample Characterization. Powder X-ray diffraction data were collected on crushed, bulk samples using a Rigaku Ultima IV X-ray diffractometer with Cu-K α radiation ($\lambda = 1.5452$ Å) over

a collection window of 5-40° in 2 θ with a step speed of 1 degree per min. Background corrected data were then compared to the patterns calculated from the CIF data for each compound to confirm that single crystals used for structure determination were representative of the bulk samples (Figures S18-S28). Combustion elemental analysis was then collected for those samples exhibiting phase purity by PXRD on a Perkin Elmer Model 2400 Elemental Analyzer. Samples, approximately 1.5-2.5 mg, were loaded into tin capsules and inserted into the combustion chamber which is monitored for C, N, and H percentages upon sample decomposition. Reported experimental values are the average of three runs. Raman spectra (Figures S45-S49) were collected for single crystals of each compound. Spectra were collected over 200-4000 cm⁻¹ using a Horiba LabRAM HR Evolution Raman Spectrometer equipped with an excitation source of 532 nm (max power = 100 mW) with 1 second incident light exposure, 20 accumulations, and a laser power of 1-3.2%. For **3A-Bi_{1-x}Eu_xCl** (x = 0.001, 0.005, 0.01, 0.05), the vibrational intensities are dwarfed by the harmonic Eu emission. Solid-state UV-Vis absorbance spectra were collected on bulk samples of those phases exhibiting PL for comparison to computational data using an Ocean Optics Flame-S-UV-Vis-ES spectrometer with a DH-2000-BAL light source and a QP400-2-SR 400 μ m diameter fiber-optic probe. Spectra (Figure S44) were recorded over a range of 200-800 nm as an average of 10 scans with integration times of 1 second.

Photoluminescent Studies. Room temperature excitation and emission spectra for the bulk samples were acquired on a Horiba PTI QM-400 Spectrofluorometer; for each phase approximately 5 mg of ground microcrystalline powder was pressed between two glass slides. Instrumental slit widths were maintained at 1-2 nm with spectral ranges of 200-500 nm for excitation and 400-800 nm for emission. Samples exhibiting visible excitation transitions were also analyzed with adjusted emission windows beginning 10 nm higher than the selected excitation

wavelengths to avoid interference (e.g., $\lambda_{\text{Ex}} = 420$, $\lambda_{\text{Em}} = 430\text{-}800$). When necessary, long pass filters were used to remove harmonic signatures. CIE 1931 chromaticity coordinates (x, y) were determined using MATLAB CIEGUI software within a spectral window of 400-800 nm for $\lambda_{\text{Ex}} = 380$ nm and 430-800 nm for $\lambda_{\text{Ex}} = 420$ nm. Coordinates for each emissive phase were plotted using OriginPro 8.5 software (Figure 16). Time-resolved lifetime measurements were acquired using a Xenon flash lamp attachment for the Horiba PTI QM-400 instrument. Luminescence decay spectra were plotted and fitted using exponential decay functions, for which lowest R^2 fits were selected. Reported decay spectra for **3A-Bi_{0.995}Eu_{0.005}Cl**, **3A-Bi_{0.99}Eu_{0.01}Cl**, and **3A-Bi_{0.95}Eu_{0.05}Cl** are plotted in Figures S37-S39 and are the average of 10,000 shots at a lamp frequency of 100 Hz. Reported lifetimes and standard deviations are the average of three separate collections.

For those compounds for which phase pure samples could not be isolated, individual single crystals were manually separated from the bulk, ground into a PMMA mixture, and pressed between glass slides at identical weights. Although residual KCl/KNO₃ impurities may exist in the bulk samples of **3A-Cl**, **3B-Cl**, and the **3A-Bi_{1-x}Eu_xCl** series ($x = 0.001, 0.005, 0.01, 0.05$), efforts were made to ensure that the luminescent behavior seen in the bulk sample could be confidently attributed to the targeted phases with no discernable influence of the trace impurities. Emission spectra for single crystals of compounds **3-Cl**, **3-Bi_{0.999}Eu_{0.001}Cl**, **3-Bi_{0.995}Eu_{0.005}Cl**, and **3-Bi_{0.99}Eu_{0.01}Cl** were acquired utilizing the aforementioned Horiba LabRAM HR Evolution Raman Spectrometer using an excitation source of 405 nm at 0.1-1% power. Emission data were collected from 425-800 nm. Consistent with the behavior of the bulk sample, the emission profiles obtained using the Raman microscope exhibited contributions from both the ligand/BiX and Eu; the Eu emission intensity was observed to become more dominant with increasing Eu doping as observed for the bulk samples. Moreover, the CIE coordinates calculated from the spectra obtained for single

crystals using the Raman microscope were in good agreement with those of the corresponding bulk sample. Unfortunately, emission spectra for single crystals of **3-Bi_{0.95}Eu_{0.05}Cl** could not be collected without oversaturating the detector. Nonetheless, the emissive features of all sample preparations - the bulk product, single crystals diluted into PMMA, and individual single crystals - are consistent with negligible or no influence from any trace impurities. A more detailed discussion along with the corresponding data that support that the trace impurities do not appreciably affect the PL behavior of the bulk samples are provided in the Supporting Information.

Computational Studies.

In an effort to gain insight into the transitions involved in the observed excitation and emission spectra, theoretical quantum mechanical calculations were performed. Structural models obtained from the single crystal structures were used to calculate the absorption spectra. Ab initio vertical absorption spectra were computed using approaches similar to those described by Sorg et al,³⁰ and in our previous work.³³ This investigation of the electronic structure properties was based on DFT calculations using the current version of the ORCA 4.2.1 program package.³⁸⁻³⁹ The CAM-B3LYP function with long-range separation was used to calculate the density of the ground state of the various sub-units.⁴⁰ The associated def2-SVP basis set was selected for all atoms,⁴¹ and a Relativistic Small Core Effective Pseudopotential was applied for Bi.⁴² The qualitative transition energies and oscillator strengths were obtained by means of a simplified version of the time-dependent DFT, sTDA (Tamm-Dancoff approach) method.⁴³⁻⁴⁵ In all calculations, spin-orbit coupling was neglected as it was found in previous work to be unnecessary to draw the main conclusions.³³ Triplet and singlet states were computed, and an energy cut-off at 5 eV was applied. Spectra were normalized over a region between 250 up to 650 nm. Note that in all spectra

representations, only the singlet states are presented. Resolution of Identity and chain-of-spheres (COSX) approximations (grid X5) were used to accelerate the calculations.⁴⁶⁻⁴⁷

RESULTS AND DISCUSSION

Structure Descriptions. Seven unique phases that are built from monomeric and/or dimeric molecular complexes were isolated through slight variation of reaction pH, stoichiometry, solvent system, and temperature. The structures generally consist of Bi-X (X = Cl, Br) sub-units with various combinations of 2,2',6',2''-terpyridine (terpy) and/or 2-thiophenecarboxylate (TC) ligand binding. Brief descriptions of the structures, including metal ion coordination environment, bond distances, and supramolecular packing interactions, are provided in order to aid the discussion of structure-property relationships. Complete tables of metal-ligand bond distances are provided as Supporting Information (Tables S1-S3). The presence and relative strength of π - π stacking interactions were qualitatively discerned based on parameters presented in reviews of chemical/biological recognition, computational modeling, and the CCDC database, with relevant face-to-face π - π stacking interactions defined as those with centroid distances of 3.4-4.0 Å and corresponding slip angles ranging from 16-40 °.⁴⁸⁻⁵⁰

Compound **1**, $[\text{Bi}_2\text{Cl}_6(\text{terpy})_2](\text{H}_2\text{O})_{0.5}$ (**1**), consists of two co-crystallized symmetrical dimers both with the general formula $\text{Bi}_2\text{Cl}_6(\text{terpy})_2$ as shown in Figure 1. Each dimer unit possesses one crystallographically unique Bi metal center which is bridged to a symmetry equivalent Bi site by two μ_2 -chlorides. Within the dimeric units, each metal center is seven coordinate bound to three nitrogens from a capping terpy and four chlorides. Bi-N and Bi-Cl distances range from 2.442-2.618(5) and 2.643-3.019(5), respectively. The bond asymmetry and a relatively “open face” directed towards the bridging chlorides of each dimer are indicative of Bi^{3+} lone pair

stereochemical activity. Though compositionally identical, there are two crystallographically unique dimers in **1**; the dimers exhibit differences in intermolecular π - π stacking and hydrogen bonding interactions. Supramolecular π - π stacking interactions exist between the terpy units from adjacent dimers; the strongest interaction exhibits a $C_{g(\text{terpy})}$ - $C_{g(\text{terpy})}$ distance of 3.554(6) Å with a slip angle (β) of 21.3°. Hydrogen bonding between neighboring water molecules and bound chlorides (Figure S9) are also present in the structure with O1(H₂)...Cl6 donor-acceptor distances of 3.218(6)-3.343(6) Å and O-H...Cl angles of 165-167°. Taken together, these intermolecular interactions result in a 3D supramolecular network of molecular dimers.

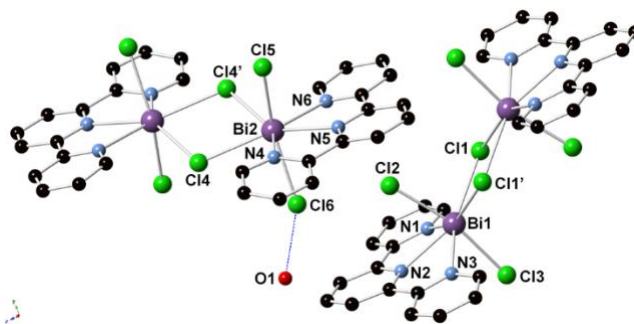


Figure 1: Illustration of the dimeric $[\text{Bi}_2\text{Cl}_6(\text{terpy})_2](\text{H}_2\text{O})_{0.5}$ complexes in **1**. Purple, green, blue, black, and red spheres are bismuth, chloride, nitrogen, carbon, and oxygen atoms, respectively. Hydrogen atoms are excluded for clarity; however, hydrogen bonding interactions between the outer-coordination sphere water and bound chloride are shown with a blue dashed line.

Compound **2**, $\text{Bi}_2\text{Cl}_4(\text{terpy})_2(\text{k}_2\text{-TC})_2$ (**2**), is built from one crystallographically unique Bi metal center. Each bismuth metal center is eight coordinated and is bound to three nitrogen atoms from a capping terpy, two oxygens from a bidentate TC, and three chlorides. As illustrated in Figure 2, two μ_2 -chlorides link two bismuth centers to form a symmetrical dimer; terpy and TC ligands cap the dimeric units. Bi-O, Bi-N, and Bi-Cl bond distances are 2.4485-2.5338(1) Å, 2.5058-2.5940(1) Å, and 2.7047-2.8655(2) Å, respectively. Weak terpy-terpy and TC-TC π - π stacking interactions

are present in the structure (Figure S10) and serve to propagate the molecular units into supramolecular 2D sheets. These interactions were tabulated in Platon,³⁷ and the strongest π - π stacking interactions have a $C_{\text{terpy}}-C_{\text{terpy}}$ of 3.7566(2) Å with $\beta = 15.1^\circ$ and $C_{\text{TC}}-C_{\text{TC}}$ of 3.8740(2) Å with $\beta = 24.2^\circ$.

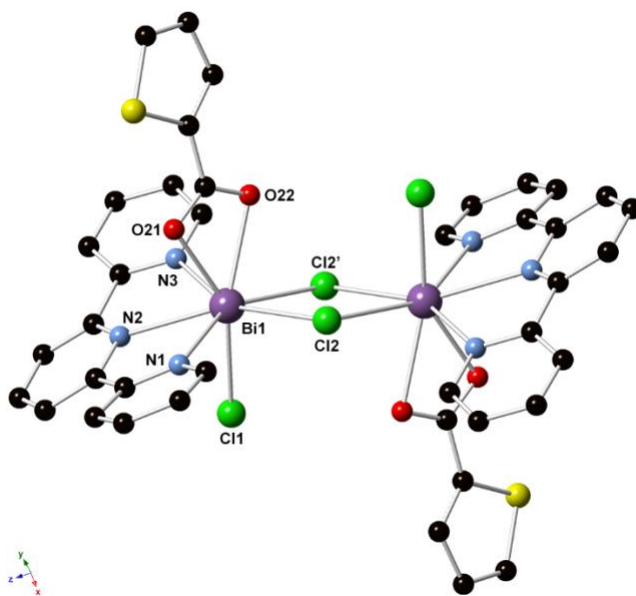


Figure 2: Illustration of dimeric unit in **2**. Purple, green, yellow, blue, black, and red spheres correspond to bismuth, chloride, sulfur, nitrogen, carbon, and oxygen, respectively. Hydrogen atoms are excluded for clarity.

The structures of compounds **3A-X** ($X = \text{Cl}, \text{Br}$), $\text{BiCl}(\text{terpy})(\text{k}_2\text{-TC})$ (**3A-Cl**) and $\text{BiBr}(\text{terpy})(\text{k}_2\text{-TC})_2$ (**3A-Br**), exhibit significant substitutional disorder of one of the TC ligands with the halide ions yet the average structure is best described as an eight coordinate Bi metal center bound to three terpy nitrogens, four oxygens from two chelating TC ligands, and a chloride ion (Figure 3). Nonetheless, as single crystal X-ray diffraction provides an average structure, in theory there are four possible Bi complexes (Figure S11) that may give rise to the observed substitutional disorder of the Cl1 and TC(31) ligands. These structural units include: **3A-Cl(a)** with one TC unit and one

Cl ion, **3A-Cl(b)** inverse coordination of one Cl and one TC unit, **3A-Cl(c)** with two chlorides, and **3A-Cl(d)** with two TC units. Further descriptions of the disorder and the refinement of **3A-Cl** are provided in Supporting Information. Distances of 2.4338-2.6793(1) Å, 2.419-2.525(1) Å, and 2.5894-2.5879(1) Å were observed for the Bi-O, Bi-N, and Bi-Cl bonds, respectively. Moderate π - π stacking interactions (Figure S12) between neighboring monomers give rise to an extensive 3D supramolecular network; $C_{g(\text{terpy})}$ - $C_{g(\text{terpy})}$ distances are 3.6064(2) Å and 3.6083(2) Å with slip angles of $\beta=23.1^\circ$ and 23.2° , respectively, while terpy-TC stacking interactions have $C_{g(\text{terpy})}$ - $C_{g(\text{TC})}$ distances of 3.6841(2) Å and 3.6877(2) Å with slip angles of $\beta=23.7^\circ$ and 23.3° . Compound **3A-Br** is isomorphous with **3A-Cl**, exhibiting the same substitutional disorder and corresponding designations, **3A-Br(a-d)**. Relevant bond distances for **3A-Br** are provided in Table S2.

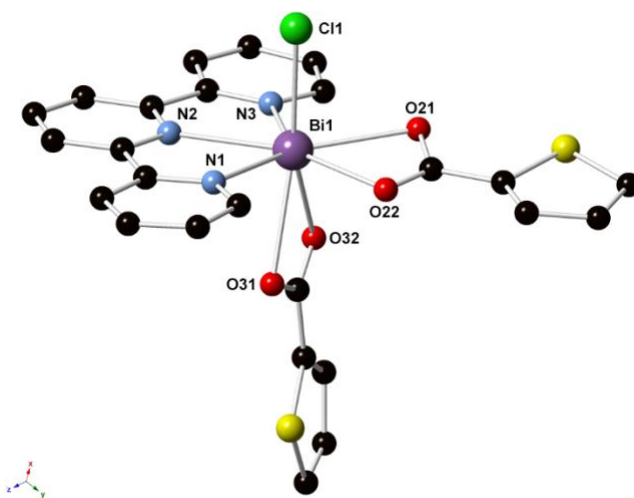


Figure 3: Illustration of the monomeric unit in **3A-Cl(a)**. Note that significant substitutional disorder of the TC and Cl ligands is present in the structure; however, this disorder has been omitted for clarity. Purple, green, yellow, blue, black, and red spheres correspond to bismuth, chloride, sulfur, nitrogen, carbon, and oxygen atoms, respectively. Hydrogen atoms are excluded for clarity.

Compound **3B-Cl**, $\text{BiCl(terpy)(k}_2\text{-TC)}_2$, is a polymorph of **3A-Cl**. Unlike **3A-Cl**, there is no evidence of substitutional disorder of the TC and Cl ligands. The structure consists of discrete monomeric units akin to those observed in **3A-Cl** that is built from an eight coordinate Bi metal center bound by three terpy nitrogen atoms, four oxygens from two bidentate TC, and a Cl atom. Bi-N, Bi-O, and Bi-Cl bond distances are 2.4394-2.6101(1) Å, 2.3857-2.6700(2) Å, and 2.6228(1) Å, respectively. More pronounced bond asymmetry in **3B-Cl** as compared to **3A-Cl** is indicative of increased Bi lone pair stereochemical activity. Furthermore, increased torsion of the terpy ligand is observed in **3B-Cl** as compared to **3A-Cl**. A summary of NCCN and CCCC torsion angles are provided in Table S4. The monomeric units are further propagated into an extended 3D supramolecular network through intermolecular terpy-terpy and terpy-TC π - π stacking interactions between adjacent monomers (Figure S13). $\text{C}_{\text{g(terpy)}}\text{-C}_{\text{g(terpy)}}$ distances and slip angles are 3.7692(2) Å and 20.3°, while $\text{C}_{\text{g(terpy)}}\text{-C}_{\text{g(TC)}}$ distances are 3.6648(2) Å and 3.7239(2) Å with slip angles of 15.2° and 25.5°, respectively.

The structure of compound **4**, $[\text{BiCl(terpy)(k}_2\text{-TC)}_2][\text{Bi(terpy)(k}_2\text{-TC)}_3]\cdot 0.55(\text{TCA})$, consists of two co-crystallized monomers with the general formulas $[\text{Bi(terpy)(k}_2\text{-TC)}_3]$ and $[\text{BiCl(terpy)(k}_2\text{-TC)}_2]$ as shown in Figure 4. A partially occupied (~55%) protonated, unbound TCA exists in the outer coordination sphere. One of the monomeric units, $[\text{Bi(terpy)(k}_2\text{-TC)}_3]$, is built from a nine coordinate Bi1 metal center that is bound to six oxygens from three bidentate TC and three nitrogens from a terpy ligand. Bi-O and Bi-N bond distances for Bi1 range from 2.4643-2.5970(2) Å and 2.5156-2.5960(2) Å, respectively. By comparison, the other monomer, $[\text{BiCl(terpy)(k}_2\text{-TC)}_2]$, consists of an eight-coordinate metal center (Bi2) which is bound to one chloride, four oxygens from two TC ligands, and three nitrogens from a capping terpy. Bi-Cl, Bi-O, and Bi-N bond distances for Bi2 range are 2.6514(2) Å, 2.4623-2.5742(2) Å, and 2.4899-2.5306(2) Å,

respectively. A complete list of metal-ligand bond distances is provided in Table S3. Hydrogen bonding is observed between outer-coordination sphere TCA (O91-H91A) and O42 with a donor-acceptor distance of 2.6400(2) Å and a O-H...O angle of 173°. Intermolecular π - π stacking interactions between the terpy ligands of adjacent monomers are also observed with the strongest exhibiting a $C_{\text{terpy}} \cdots C_{\text{terpy}}$ distance of 3.6209(2) Å with a slip angle (β) of 15.6°. Taken together these π - π stacking interactions link monomeric units into 1D supramolecular chains (Figure S14).

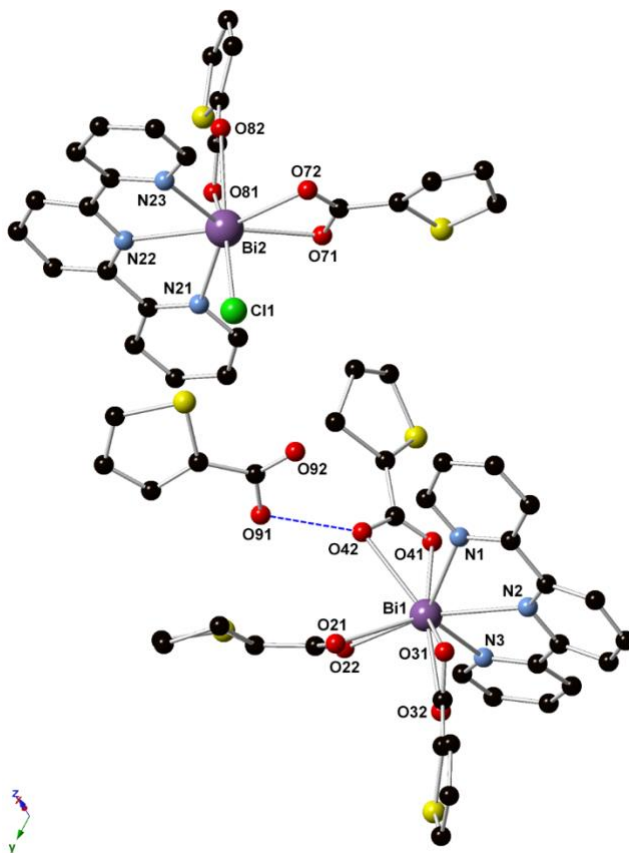


Figure 4: Illustration of the monomeric complexes observed in **4**. Purple, green, yellow, blue, black, and red spheres correspond to bismuth, chloride, sulfur, nitrogen, carbon, and oxygen atoms. Hydrogen atoms are excluded for clarity; however, hydrogen bonding interactions are displayed with a blue dashed line between outer coordination sphere TCA -OH group and bound TC carboxylate oxygen atoms.

The structure of compound **5**, $[\text{BiBr}_3(\text{terpy})(\text{MeOH})]$, consists of two crystallographically distinct monomers of the same general formula $[\text{BiBr}_3(\text{terpy})(\text{MeOH})]$ (Figure 5). One of the monomers contains a seven coordinate metal center, Bi1, which is bound to three bromides, three nitrogens from a tridentate terpy, and one oxygen from methanol. Bi-Br, Bi-O, and Bi-N bond distances within this unit are 2.7742-2.9054(2) Å, 2.6280(2) Å, and 2.4723-2.6061(2) Å, respectively. The Bi metal center, Bi2, in the other crystallographically distinct monomeric complex has the same local coordination environment as that observed for Bi1; Bi-Br, Bi-O, and Bi-N distances are 2.7610-2.9491(1) Å, 2.6474(2) Å, and 2.4887-2.5724(2) Å, respectively. Intermolecular stacking interactions are observed between terpy ligands of neighboring monomers with $C_{\text{terpy}}-C_{\text{terpy}}$ distances of 3.5556-3.8506(3) Å and corresponding slip angles (β) of 14.8-23.7°. Interestingly, these $\pi-\pi$ stacking interactions only exist between like monomers. Overall, the monomers containing Bi1 produce a 2D supramolecular sheet through $\pi-\pi$ stacking interactions. By comparison, the monomers built from Bi2 are linked into supramolecular 1D chains along [100] via $\pi-\pi$ stacking interactions of the capping terpy ligands. Hydrogen bonding between the bound halide and water molecules of the Bi1 and Bi2 monomeric complexes are observed with O41-H41 \cdots Br4 and O51-H51 \cdots Br3 donor-acceptor distances and angles of 3.2057(3) and 3.3320(3) Å and 163 and 176°, respectively. Packing diagrams of **5** that further illustrate these hydrogen bonding interactions are provided in the Supporting Information (Figures S15-S16).

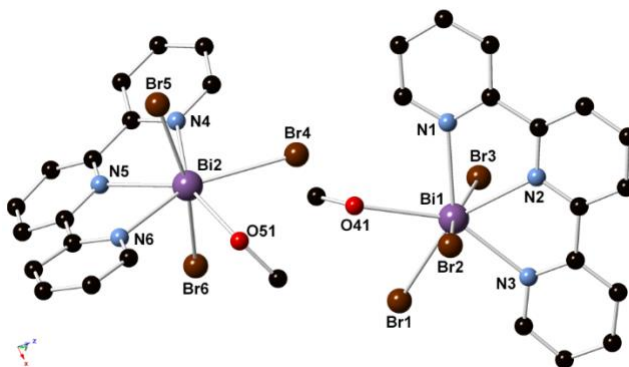


Figure 5: Illustration of the co-crystallized monomeric complexes in **5**. Purple, brown, blue, black, and red spheres correspond to bismuth, bromide, nitrogen, carbon, and oxygen atoms, respectively. Hydrogen atoms are excluded for clarity.

The structure of compound **6**, $[\text{BiBr}_2(\text{terpy})(\text{k}_2\text{-TC})][\text{BiBr}_{1.16}(\text{terpy})(\text{k}_2\text{-TC})_{1.84}]$, consists of two co-crystallized monomers as illustrated in Figure 6. The monomeric complexes have the general formulas $[\text{BiBr}_2(\text{terpy})(\text{k}_2\text{-TC})]$ and $[\text{BiBr}_{1.16}(\text{terpy})(\text{k}_2\text{-TC})_{1.84}]$. The first complex, $[\text{BiBr}_2(\text{terpy})(\text{k}_2\text{-TC})]$, is built from a seven coordinate Bi1 metal center bound to two Br atoms, two oxygens from a bidentate TC, and three nitrogens from a capping terpy ligand. This unit is isostructural one of the complexes, **3A-Br(c)**, described previously. Bi-Br, Bi-O, and Bi-N bond distances for Bi1 range from 2.7954-2.8501(2) Å, 2.4859-2.5276(2) Å and 2.4565-2.5292(2) Å, respectively. The second complex, $[\text{BiBr}_{1.16}(\text{terpy})(\text{k}_2\text{-TC})_{1.84}]$, exhibits substitutional disorder of the Br and TC substituents; the number of bound bromides and TC refined to 1.16 and 1.84 per bismuth metal center. Overlapping Br and TC positions are shown in Figure S8. As a result of this disorder, Bi2 may be described as a seven or eight coordinate complex, depending on the occupancy of the Br/TC units. Given the low partial occupancy of Br5 and Br6, combined ~16 %, we describe the complex here as eight coordinate for the sake of discussion. The Bi2 metal center is bound to one Br, four oxygens from two TC units, and three nitrogens from a capping terpy. Bi-Br, Bi-O, and Bi-N bond distances for Bi2 range from 2.8144-2.9871(2) Å, 2.3928-2.7380(2) Å, and 2.4453-2.5053(2) Å, respectively. Significant bond asymmetry as well as the presence of an apparent “open” face directed trans to N4 is evident of appreciable Bi lone pair stereochemical activity. A complete listing of metal-ligand bond distances is provided in Table S3. Intermolecular π - π stacking interactions between terpy and/or TC ligands of adjacent monomers is observed (Figure S17); the strongest of these interactions has a $\text{C}_{\text{Terpy}}\text{-C}_{\text{Terpy}}$ distance of 3.7147(2) Å and a

slip angle (β) of 22.9° . Interactions between the terpy and thiophene rings are also observed with $C_{\text{terpy}}-C_{\text{TC}}$ distances of $3.7625(2) \text{ \AA}$ and $3.8236(2) \text{ \AA}$ with corresponding slip angles (β) of 23.3 and 25.0° . Intermolecular $\pi-\pi$ stacking between TC units have a $C_{\text{TC}}-C_{\text{TC}}$ distance of $3.6832(2) \text{ \AA}$ with a slip angle of 18.5° . Overall, these stacking interactions link the monomeric complexes into a 3D supramolecular network.

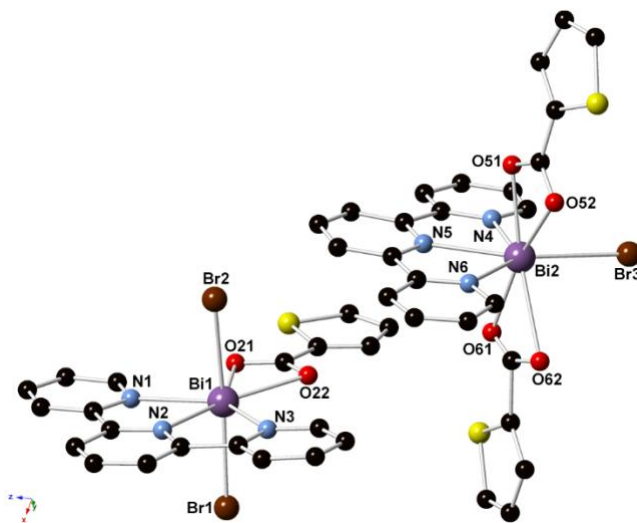


Figure 6: Illustration of the monomeric units in **6**. Note that for the sake of clarity, partial occupancy of the Br/TC units bound to Bi2 is not shown. Purple, brown, yellow, blue, black, and red spheres correspond to bismuth, bromide, sulfur, nitrogen, carbon, and oxygen atoms, respectively. Hydrogen atoms are excluded for clarity.

Synthesis and Design Considerations.

In this work, 2,2',6',2''-terpyridine (terpy) and 2-thiophene monocarboxylate (TC) were used as ligands. In addition to possessing intrinsic luminescent properties, these ligands were chosen for their propensity to adopt chelating binding modes that would likely restrict the dimensionality of the resultant metal complexes to discrete molecular species rather than extended networks.

Molecular species are of particular interest as they provide a platform for building fundamental knowledge of structure property relationships; the individual structural motifs along with the supramolecular interactions that underpin unique luminescent behaviors may be elucidated thus informing materials design for molecular and extended networks alike. Furthermore, our prior research efforts employing these ligands in Ln-, Bi-, and Ln doped Bi-based compounds provides analogous systems from which a more in-depth understanding of structure-property relationships may be understood.⁵¹⁻⁵²

Relatively mild synthetic conditions afforded a structurally diverse catalog of Bi-halide-organic compounds. Terpyridine effectively “capped” the Bi coordination sphere in all of the phases reported herein. By comparison, TC and halide ions exhibited competitive Bi binding; deprotonation of the TCA was achieved through pH adjustment of the reaction solution. Absent pH adjustment of the reaction solution, the TCA likely remained protonated and did not coordinate the bismuth metal center. This was evidenced in the synthesis of compound **1**, $[\text{Bi}_2\text{Cl}_6(\text{terpy})_2](\text{H}_2\text{O})_{0.5}$, that formed under acidic solution conditions, without the addition of base and for which no evidence of TC complexation was observed (Figure S18). Indeed, without sufficient base additions compound **1** was often observed as an unwanted coprecipitate in the synthesis of compounds **3A-Cl**, **3B-Cl**, and **4**. Similarly, no or insufficient pH adjustment during the synthesis of **6** would lead to the undesired formation of **5**.

While pH served as a critical synthetic handle to control Bi-TC ligand complexation, the limited solubility of Bi salts posed a significant challenge in obtaining phase pure products. With respect to phase purity, the general insolubility of bismuth compounds resulted in an arduous synthetic landscape, with unwanted coprecipitates, mixed phase products, and crystal twinning often

observed. Slight variations in the synthetic conditions including metal to ligand stoichiometry, temperature, solvent, reaction time were thus examined.

For the phases containing BiCl subunits (**2**, **3A-Cl**, **3B-Cl**, and **4**), reaction time, metal to ligand ratio, and solvent were determinant factors in the compound that formed. Polymorphs **3A-Cl** and **3B-Cl** were obtained under nearly identical synthetic conditions with reaction time as the only variable. Whereas the kinetic product, **3A-Cl**, could be isolated within minutes of mixing the reactants, compound **3B-Cl** formed when the reaction was allowed to proceed for hours. For these phases, a ratio of 1 BiCl₃: 1 terpy: 3 TCA was used. Notably, this ratio is not consistent with the stoichiometry observed in the final product, BiCl(terpy)(TC)₂. However, efforts to prepare BiCl(terpy)(TC)₂ stoichiometrically resulted in the coprecipitation of **3A-Cl** and **2**, Bi₂Cl₄(terpy)₂(k₂-TC)₂. A phase pure product of **2** was obtained at a reaction stoichiometry of 1 BiCl₃: 1 terpy: 1 TCA which is consistent with the composition of **2**.

While **3A-Cl** and **3B-Cl** were isolated from methanolic solutions, compound **4**, [BiCl(terpy)(k₂-TC)₂][Bi(terpy)(k₂-TC)₃]•(TCA), was prepared under aqueous conditions. The solvent system was also an important factor in isolating the bromide phase as the synthetic conditions used to isolate the chloride phases were not directly transferable to the bromide analogs. Unlike **3A-Cl**, compound **3A-Br** was obtained from an aqueous reaction solution. Furthermore, compound **6**, [BiBr₂(terpy)(k₂-TC)][BiBr_{1.16}(terpy)(k₂-TC)_{1.84}], was isolated from a methanol solution with mild heating. Without this additional adjustment in reaction temperature, **3A-Br** and **6** were obtained as coprecipitates. Full details of the optimal synthetic parameters used to isolate each phase are presented in the Supporting Information.

The overall specificity of the synthetic conditions required to achieve phase purity for the compounds reported herein alludes to a complicated reaction landscape that through careful

control, yielded a structurally diverse catalog of compounds. Importantly, the reported phases provide solid-state snapshots of varied Bi-organic and Bi-halide complexation that coupled with electronic structure calculations afford insight into the structural underpinnings of distinct luminescent features.

Luminescent Behavior of the Homometallic Phases

The solid-state photoluminescent behavior of the reported materials was examined via steady-state and time-dependent methods. Compounds **2**, **3A-Cl**, **3A-Br**, **3B-Cl**, **4**, and **6** exhibited yellow-green to yellow emission, with broad transitions centered at 533 to 560 nm (Figure 7). Individual spectra are provided in the Supporting Information as Figures S29-S34.

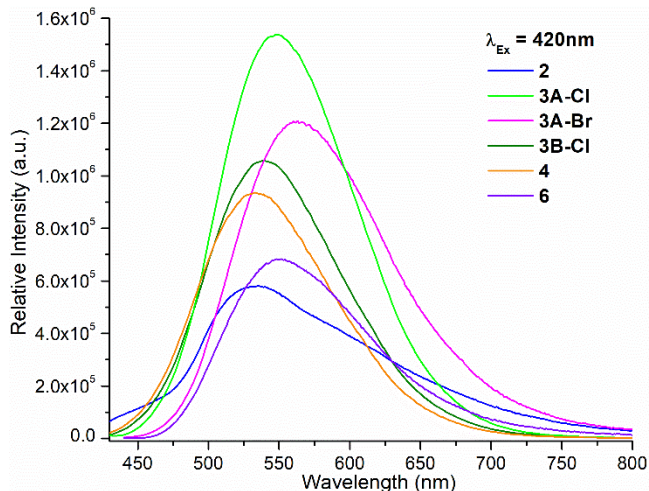


Figure 7: Emission spectra for bulk samples of **2**, **3A-Cl**, **3A-Br**, **3B-Cl**, **4**, and **6** at an excitation ($\lambda_{\text{Ex}} = 420$ nm).

Shifts in the emission maxima were observed and attributed to slight variations in ligand orientation, halide identity, and/or supramolecular packing as seen in other hybrid materials.⁵³⁻⁵⁵ Interestingly, comparison of the emission spectra of polymorphs **3A-Cl** and **3B-Cl** revealed a shift of approximately 10 nm in the peak maximum. This shift is consistent with visual inspection of

the samples under a UV hand lamp, for which the emission of **3B-Cl** ($\lambda_{\text{max}} = 540$ nm) was noticeably greener than **3A-Cl** ($\lambda_{\text{max}} = 550$ nm) emission. Additionally, a bathochromic shift in emission was observed in the spectra of isomorphous compounds **3A-Cl** and **3A-Br** ($\lambda_{\text{max}} = 560$ nm). Unfortunately, time-dependent luminescent decay studies for these homometallic Bi halide phases revealed lifetimes below the reliable detection limits of our instrument ($\tau = <10$ μs). Broad emission with short emission decay lifetimes have similarly been reported for other Bi-halide and Bi-organic materials.⁵⁶⁻⁵⁸ By comparison, the excitation spectra for the homometallic phases, **2**, **3A-Cl**, **3A-Br**, **3B-Cl**, **4**, and **6**, exhibited relatively rare profiles, with excitation extending into the visible region (Figure 8).

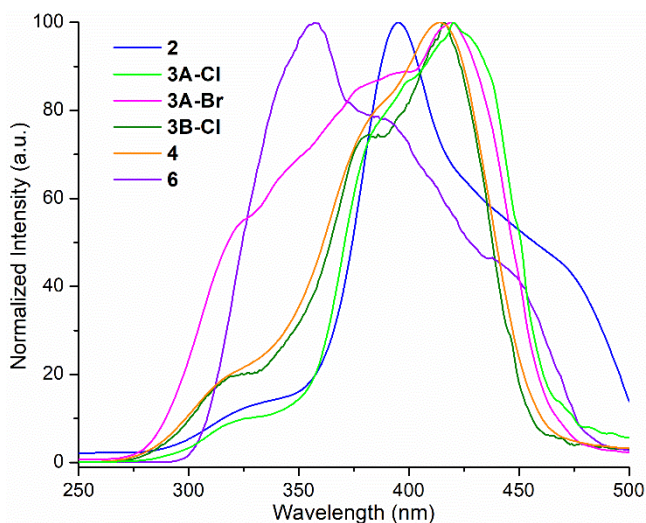


Figure 8: Normalized excitation spectra for **2**, **3A-Cl**, **3A-Br**, **3B-Cl**, **4**, and **6**.

As shown in Figure 8, the excitation spectra for **2**, **3A-Cl**, **3A-Br**, **3B-Cl**, **4**, and **6** all exhibit an onset at approximately 280 nm but vary in overall profile. Notably, for all of these compounds the excitation profiles extend into the visible region. The spectra of polymorphic compounds **3A-Cl** and **3A-Br** show no significant shifting of excitation maxima ($\lambda_{\text{max}} = 420$ nm); however, more pronounced intensity is seen at lower wavelengths (300-360 nm) for **3A-Br**. Similarly, for the

BiBr phase, **6**, the most intense excitation features are observed at lower wavelengths with a maximum excitation wavelength of 360 nm.

Comparison of the excitation spectra of isostructural compounds **3A-Cl** and **3A-Br** suggests that halide identity has little bearing on how far into the visible region excitation may be achieved. By contrast, the relative number of complexed halide ions per metal center appears to be a significant factor on extension of the excitation profile into the visible region across the compounds reported herein. For example, comparison of the excitation spectra of **2**, **3A-Cl**, and **3B-Cl** shows that whereas excitation extends out to 500 nm for **2**, little intensity is observed past 470 nm and 450 nm for **3A-Cl** and **3B-Cl**, respectively. The numbers of bound chloride ligands per Bi metal center are three, one, and one for **2**, **3A-Cl** and **3B-Cl**, respectively. While visible excitation has been achieved in several other Bi halide hybrid materials, the origin of these transitions, as well as the resultant emission, has been difficult to discern from photoluminescent data alone.^{7, 59} The photoluminescent behavior of bismuth-based materials has been attributed to a number of pathways including metal centered (MC) transitions, metal-to-ligand/ligand-to-metal charge transfer (MLCT/LMCT), and/or intra- or interligand charge transfer (ILCT/LLCT).^{26, 29-31, 60} Thus, in an effort to identify the transitions, orbital contributions, and corresponding structural motifs that underlie the luminescence observed for **2**, **3A-Cl**, **3A-Br**, **3B-Cl**, **4**, and **6** as well as elucidate trends in the observed PL spectra, parallel computational efforts were employed.

Structural cut-outs, derived from the single crystal structural data for compounds **2**, **3A-Cl**, **3A-Br**, **3B-Cl**, and **6**, were rendered and used as models for quantum mechanical calculations. For all compounds, the experimental absorption bands could be accounted for using isolated molecular units which for compounds **3**, **4**, and **6** are monomers and for compound **2**, is a dimer. The theoretical UV-Vis absorption spectra were calculated and compared to the experimentally

obtained optical absorption spectra (Figures S44, S50, S54, S55, S56). Overall, all of the modeled structures containing halide substituents exhibited absorption features that extended into the visible region (400+ nm), consistent with the experimental absorption spectra. These computational results are provided in the Supporting Information; however, herein we discuss compound **3A-Br** as this phase best illustrates the features and trends exhibited by the reported compounds. Due to substitutional disorder of the metal bound bromide and TC ligands in **3A-Br** (Figure S11), multiple structural cut-outs, including BiBr(terpy)(TC)₂ [**3A-Br(a)**], BiBr₂(terpy)(TC) [**3A-Br(c)**], and Bi(terpy)(TC)₃ [**3A-Br(d)**], were modelled to explore the influence of changes in the Bi local coordination environment on the resulting spectra. Cut-out **3A-Br(b)** was not included since it is structurally equivalent to **3A-Br(a)**. The theoretical absorption spectra with the singlet-state transitions for these species are displayed in Figure 9.

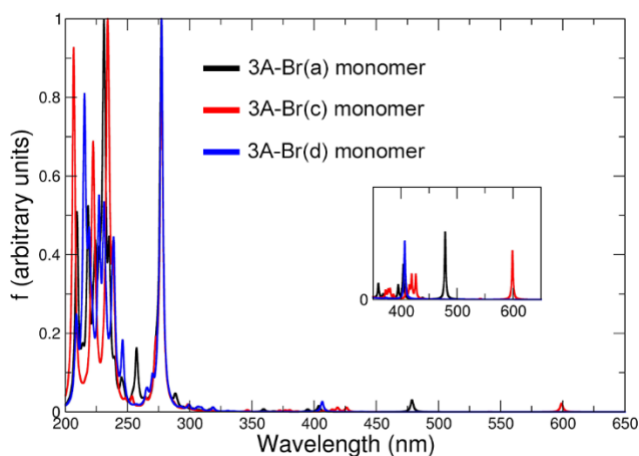


Figure 9: Theoretical absorption spectra for associated singlet state transitions for monomeric species BiBr(terpy)(TC)₂ [**3A-Br(a)**], BiBr₂(terpy)(TC) [**3A-Br(c)**], and Bi(terpy)(TC)₃ [**3A-Br(d)**]. Inset spectra show zoomed in region of interest (350-650 nm).

The spectra of the monomeric model complexes all exhibit transitions between 200-350 nm consistent with intra- and interligand transitions. However, above 350 nm notable differences are observed (Figure 9, inset) that may be attributed to differences in local coordination environment.

The energies of all significant ground state (GS) to singlet excited state transitions between 315-600 nm are summarized in Table 2. Further, the frontier orbital contributions for **3A-Br(a)**, **3A-Br(c)**, and **3A-Br(d)** are shown in Figures 10, 11, and 12, respectively.

Table 2: Absorption energies of frontier orbital transitions for **3A-Br(a)**, **3A-Br(c)**, and **3A-Br(d)**. The orbital model (OM) numbers for each structural derivative are denoted for occupied (Occ.) and virtual (V.) orbital contributions and correspond to those shown in Figures 10-12.

State	3A-Br(a)		Figure 10		3A-Br(c)		Figure 11		3A-Br(d)		Figure 12	
	Energy (eV)	(nm)	OM Occ.	OM V.	Energy (eV)	(nm)	OM Occ.	OM V.	Energy (eV)	(nm)	OM Occ.	OM V.
1	2.60	479	9	1	2.07	598	6	1	3.05	407	10	1
2	2.83	438	9	2	2.30	540	6	2	3.33	372	10	2
3	3.07	404	8	1	2.91	425	5	1	3.70	335	3 5, 8	1
4	3.14	395	7	1	2.96	419	4	1	3.75	331	2 7, 3	1
5	3.37	368	8	1	2.99	414	3	1	3.89	319	1 5, 8	1
6	3.45	359	7	2	3.03	408	2	2	-	-	-	-
7	3.61	343	2	1	3.21	387	5	2	-	-	-	-
8	3.89	319	1 2, 3	1 2, 1	3.26	381	4	2	-	-	-	-
9	3.92	316	2 2, 3	2 1, 1	3.29	376	3	2	-	-	-	-
10	-	-	-	-	3.34	372	2	2	-	-	-	-
11	-	-	-	-	3.42	363	4	3	-	-	-	-
12	-	-	-	-	3.58	346	6	3	-	-	-	-

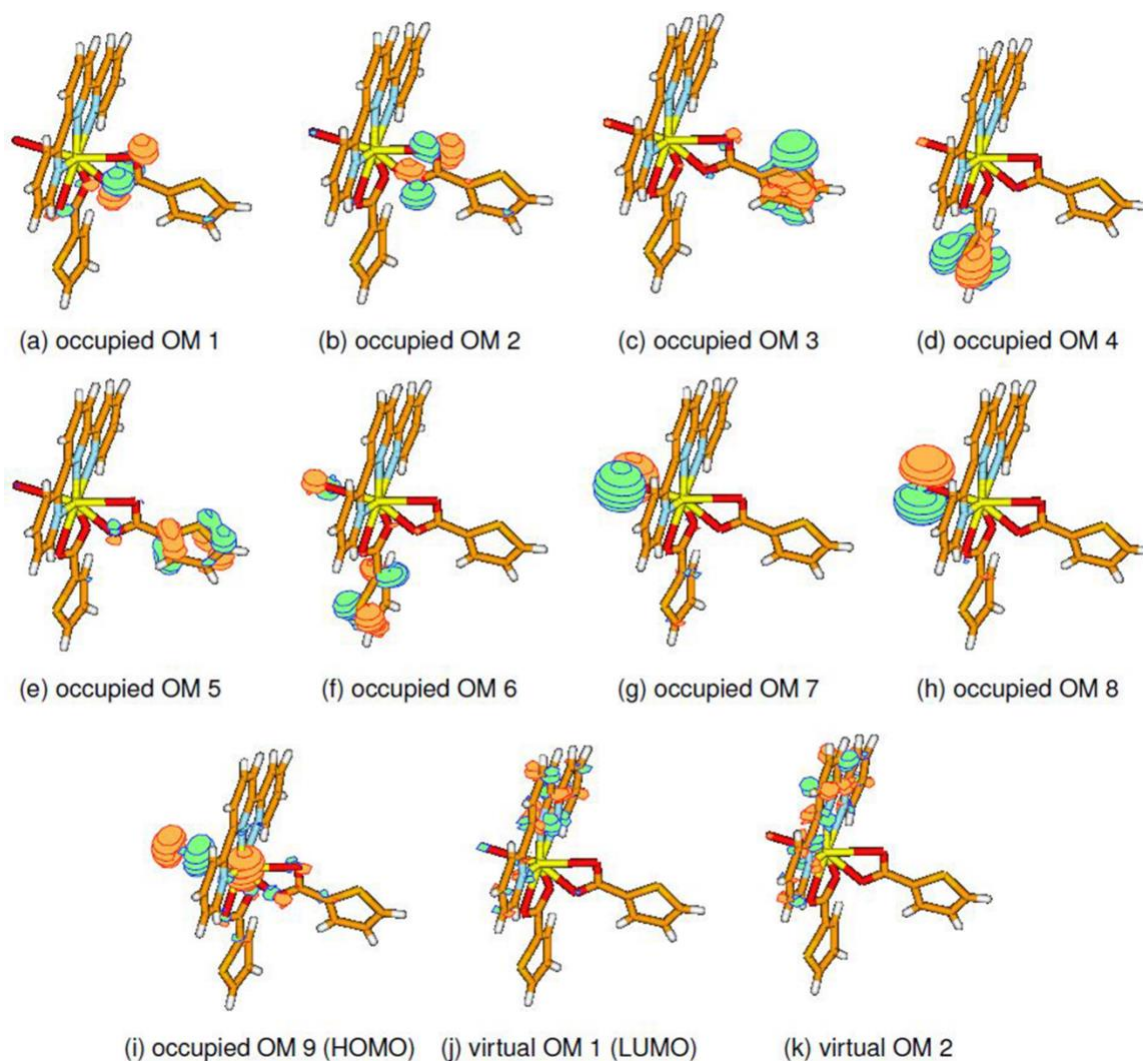


Figure 10: Calculated molecular orbital diagram for relevant **3A-Br(a)** energy states involved in the transitions observed between 315-650 nm.

For **3A-Br(a)**, the lowest energy absorption occurs at 479 nm and originates from a transition from the highest occupied molecular orbital (HOMO) to the lowest unoccupied molecular orbital (LUMO). As depicted in Figure 10(i), the HOMO mainly consists of the 6s orbital of the Bi and the p_z orbital of bromide with some contribution from the non-bonding orbitals of the TC group trans to the Br. Such mixed contributions emphasize a cooperative metal-halide energy state. As shown in Figures 10(j) and 10(k), the LUMO and the LUMO+1 states are π^* orbitals of bound

terpy. Therefore, the calculated absorbance band and the corresponding experimentally observed excitations in the visible region are attributed to a metal-halide subunit to ligand charge transfer (XMLCT). Notably, all of the bands between 350-450 nm correspond to excitations out of occupied orbitals solely exhibiting halide orbital identity. Such contributions suggest intramolecular halide to ligand charge transfer (XLCT) mechanisms may also give rise to the excitations seen in the experimental data. Finally, the absorbance bands below 350 nm demonstrate TC to terpy based transitions which suggest ligand-to-ligand charge transfer (LLCT) pathways. Therefore, the absorptions/excitations between 315-600 nm, result from various types of transitions that are facilitated by a harmonious concert of metal, halide, and organic orbital interactions. Although the broad emission bands for the homometallic phases (Figure 7) are reminiscent of ligand and/or Bi^{3+} centered transitions, the origin of the emission is likely attributed to a ligand to metal-halide subunit charge transfer (LXMCT) given the low energy of the calculated XMLCT excitations relative to other charge transfer, intramolecular, or intra-atomic transitions. Alternatively, relaxation from the terpy π^* (LUMO) $\rightarrow \pi$ could also serve as a potential route for the observed emission.

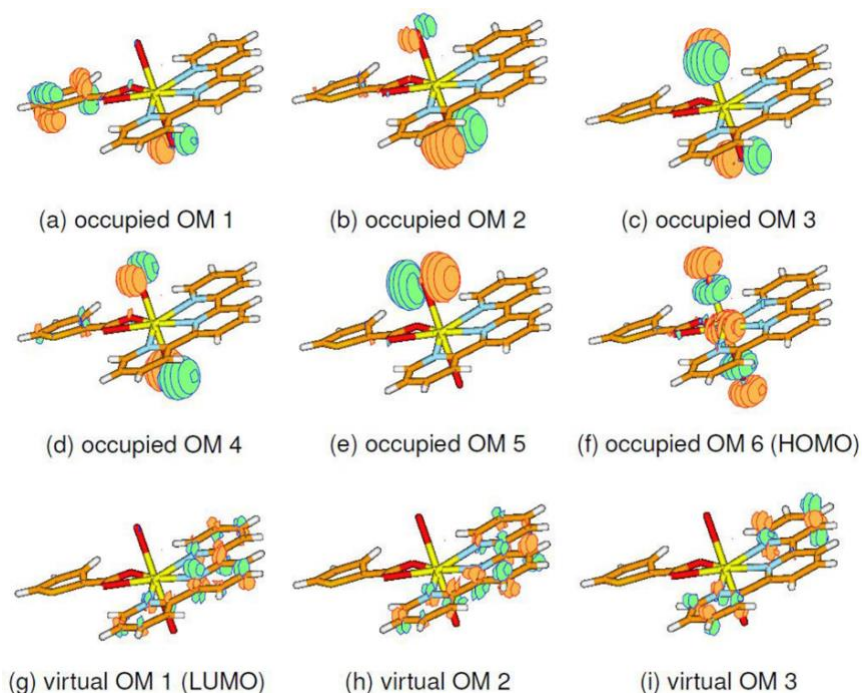


Figure 11: Calculated molecular orbital diagram for relevant **3A-Br(c)** energy states for transitions between 315-650 nm.

For **3A-Br(c)**, the lowest energy transition calculated at 598 nm also originates from a HOMO \rightarrow LUMO transition. As depicted in Figure 11(f), the HOMO shows significant contributions of the 6s orbital of the Bi and the p_z orbitals of both bromides. Once again, terpy π^* orbitals serve as the virtual LUMO states as shown in Figure 11(g-i). Therefore, the calculated visible absorbance is assigned to a XMLCT pathway. As compared to **3A-Br(a)** which only possesses a single Br substituent, the **3A-Br(c)** derivative possesses a trans BiBr₂ sub-unit. An increasing number of halide substituents on Bi that are able to interact with the unoccupied terpy π^* orbitals, likely results in a more delocalized HOMO, characterized by mixing of the Bi s and Br p orbitals with antibonding character. Based on this molecular orbital character, the anticipated higher energy of the HOMO as compared to underlying occupied bonding orbitals would have associated decreases in transition energy to the LUMO, and a subsequent bathochromic shift of absorbance further into

the visible region. Remarkably, this relationship between halide coordination and visible excitation is reflected in the experimental excitation spectra of the reported compounds.

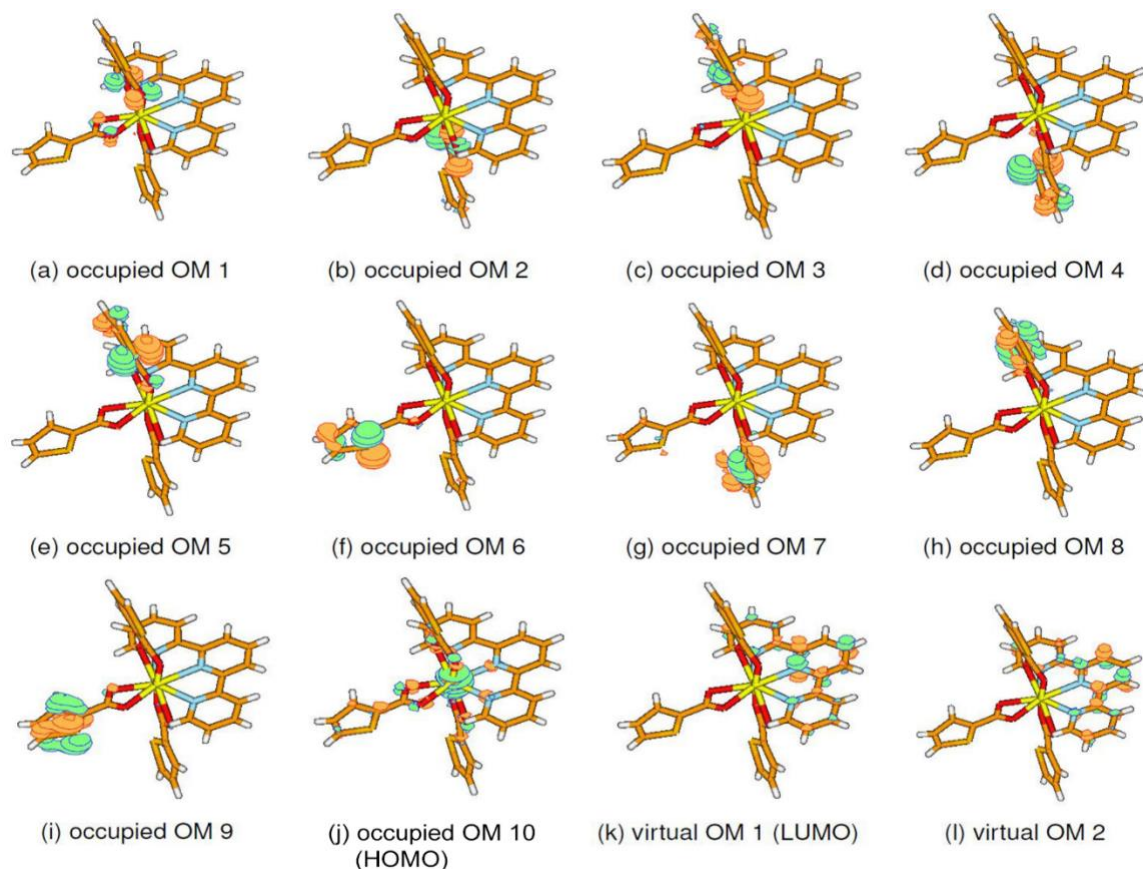


Figure 12: Calculated molecular orbital diagram for relevant **3A-Br(d)** energy states for transitions between 315-650 nm.

For **3A-Br(d)**, no calculated absorption transitions were observed beyond 407 nm. As illustrated in Figure 12, the main orbital contributions for the few calculated absorbances observed suggest that these transitions may originate from independent intramolecular metal-to-ligand charge transfer (MLCT) and LLCT pathways. The notable absence of visible absorbance bands absent halide coordination further corroborates that the BiX sub-unit serves as the essential structural motif for obtaining visible excitation as well as the resulting emission. It is worth noting that we previously reported a homometallic Bi(terpy)(k₂-TC)₃ compound that is isostructural to **3A-Br(d)**;

this phase not only lacked visible excitation but also did not possess any appreciable luminescence.⁵² Taken together, this suggests that for an otherwise non-luminescent Bi complex (i.e. Bi(terpy)(TC)₃), halipurede substitution may unlock unique luminescent properties. It is worth noting that all of the structural models for **3A-Cl**, **3A-Br**, **3B-Cl**, and **6** that contain a BiX sub-unit exhibit visible absorbance bands in the calculated spectra, which is consistent with the experimental excitation spectra.

Structural cut-outs of **3A-Cl**, akin to those described for **3A-Br**, were also modelled in an effort to examine the effects of halide identity on the energy of the calculated transitions. The calculated absorbance spectra for **3A-Cl(a)**, **3A-Cl(c)**, and **3A-Cl(d)** are shown in Figure S50. The corresponding energies are provided in Table S5 and the molecular orbital designations are illustrated in Figures S51-53. The presence and extension of absorptions into the visible region for the **3A-Cl** derivatives appears to similarly depend on the existence and number of metal-bound halides in the complex. The lowest energy absorptions calculated for **3A-Cl(a)** and **3A-Cl(c)** correspond to transitions from the HOMO consisting of mixed Bi and chloride orbital contributions to the LUMO virtual states that are solely terpy π^* orbitals. For the halide substituted complexes, the transitions calculated above 380 nm for the **3A-Cl** derivatives are consistent with those calculated for the isomorphous **3A-Br**. The calculated absorbance spectra for **3A-Cl(a)** and **3A-Br(a)** are shown in Figure S54. Comparison of the spectra reveals that the BiBr derivative exhibits more absorption bands at lower wavelengths (i.e., 316 and 319 nm) than the BiCl analog; this is in good agreement with the general shape of the experimental excitation profiles. The prominence of higher energy transitions (300-400 nm) within BiBr phases, as well as low-energy absorptions that extend into the visible range, is further reflected in the calculated absorbance spectrum of compound **6** (Figure S55).

Slight shifts that are observed in the experimental excitation spectra of **3A-Cl** and **3B-Cl** are also accounted for by the computational results. As shown in [Figure S57](#), the calculated absorption spectra for the isostructural compounds **3A-Cl(a)** and **3B-Cl** reveal a shift in the lowest energy transition. This shift is attributed to differences in TC ligand orientation and Bi-Cl bond lengths, observed both experimentally and computationally, that likely originate from the increased stereochemical activity of the Bi 6s occupied orbital in **3B-Cl** as compared to **3A-Cl**. Alternatively and/or in concert with the distortion of the metal center, increased torsion of the terpy ligand as observed in **3B-Cl** away from the more planar motif seen in **3A-Cl** may also contribute to the observed shifting given the relevance of the terpy π^* orbitals to the LUMO. Similar increases in π^* energy with increasing torsion of bipyridine substituents have been observed.⁶¹ The shifting of the calculated, visible absorption band is consistent with that seen in the experimental excitation and absorbance spectra, wherein the lowest energy absorptions for **3B-Cl** are slightly blue shifted as compared to those observed for **3A-Cl(a)**. Analysis of monomer cutouts derived from **6** further support the relationship between the Bi-X bond distance and/or associated distortions about the metal center and shifts in the calculated and experimental data ([Figure S55](#)). These discrete changes in structure and absorbance highlight the sensitive, yet potentially tunable interplay of ligand identity/orientation, stereochemical activity of the Bi metal center, subsequent energetic pathways, and overall luminescent behavior.

Finally, to assess the potential impacts of supramolecular packing interactions on the excitation and emission spectra, pseudo-oligomeric cut-outs of **3A-Br** were rendered that captured the relevant intermolecular π - π stacking interactions derived from the crystallographic data. Comparison of the calculated transition energies and absorbance spectra of the monomeric unit to those of pseudo- dimeric, trimeric, tetrameric, pentameric, and hexameric models revealed no

major changes in the higher energy (200-350 nm) absorption features. However, significant blue shifting of the absorbance bands between 350-600 nm was observed with increasing size of the pseudo-oligomer. The calculated absorbance spectra for the monomer and pseudo-hexamer models of **3A-Br(c)** are shown in Figure 13, with the lowest energy absorptions for the monomer and hexamer calculated at 600 and 460/525 nm, respectively.

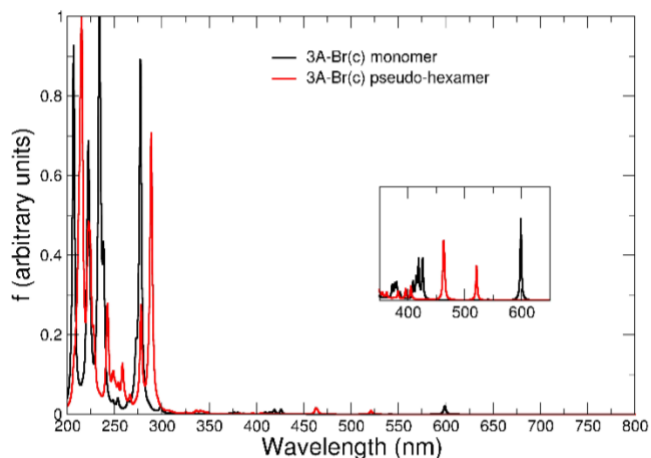


Figure 13: Theoretical absorption spectra for associated singlet state transitions for monomer and pseudo-hexamer units of **3A-Br(c)**. Sub-set spectra highlight region of interest (350-650 nm)

This shift of approximately 75 nm emphasizes the necessity of having a large enough system modelled to reproduce the positioning of the bands of the experimental data more accurately. However, regardless of positioning, the structural origins of these visible absorption bands were found to be identical and very localized to intramolecular transitions between the BiX and organic ligand sub-structures of the individual complexes. Since our primary aim was to characterize the origins of these low-lying bands, the prior discussion and calculated data were justifiably limited and simplified to the monomer representation of the Bi halide organic compounds. Moving forward, these visible absorptions of interest were exploited to further achieve interesting luminescent properties in heterometallic phases.

Photoluminescent Color Tuning in Eu Doped Samples.

The photoluminescent behavior of a Eu doped heterometallic series, **3A-Bi_{1-x}Eu_xCl** ($x = 0.001, 0.005, 0.01, 0.05$), was investigated. The excitation and emission spectra of compound **3A-Bi_{0.995}Eu_{0.005}Cl**, which is representative of the series, are shown in Figure 14. Examination of the excitation profile reveals three predominant features with maxima at approximately 320, 380, and 420 nm, with the most intense peak falling in the visible range, as was observed for the homometallic analog **3A-Cl**. Furthermore, this excitation pathway can be utilized to obtain dual emissive features.

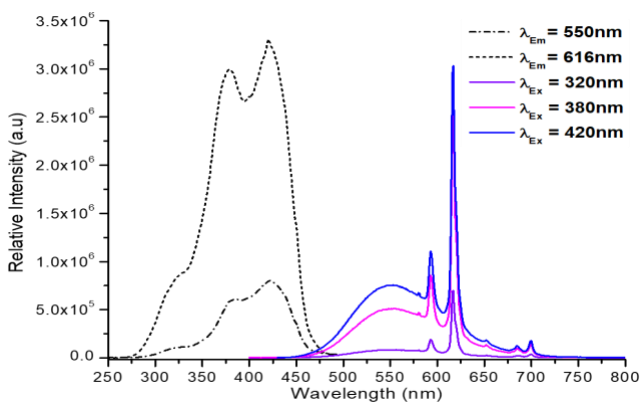


Figure 14: Relative excitation (dashed line) and emission (solid line) spectra for compound **3A-Bi_{0.995}Eu_{0.005}Cl** at the specified wavelengths of interest.

Characteristic Eu emission is observed with the peak of maximum intensity centered at 616 nm which corresponds to the $^5D_0 \rightarrow ^7F_2$ transition. Transitions to the 7F_0 , 7F_1 , 7F_3 , and 7F_4 energy levels are seen at 582, 593, 652, and 680-705 nm, respectively. Such intense emissions confirm effective sensitization of the Eu metal center doped into the Bi host. Eu sensitization is likely facilitated through the “antenna effect”,^{18, 62} however, charge transfer pathways may also act to sensitize the

Eu emission. In addition to the sharp Eu centered transitions, a broad underlying emissive feature centered at 550 nm is observed. The profile of this broad band and its position are consistent with that of the homometallic phase, **3A-Cl**, and likely originates from similar ligand/LXMCT energetic transitions. Interestingly, the relative intensities of the sharp Eu transitions and the broad-band emission of the **3A-Bi_{1-x}Eu_xCl** ($x = 0.001, 0.005, 0.01, 0.05$) series can be controlled compositionally through the amount of Eu doping. As illustrated in Figure 15, increased Eu incorporation results in more dominant and intense Eu emission. As a result, photoluminescent color tuning (PLCT) from yellow-green emission in the homometallic Bi phase to red emission at only 5% Eu doping in **3A-Bi_{0.95}Eu_{0.05}Cl** was achieved. Compound **3A-Bi_{0.999}Eu_{0.001}Cl** demonstrates the greatest contribution of ligand/LXMCT based emission within the heterometallic series and subsequently produced the highest degree of color tuning away from characteristic red Eu³⁺ emission. Images of emission from the bulk samples under a UV handlamp ($\lambda_{\text{Ex}} = 365 \text{ nm}$) are provided in Figure S43. While compositional based PLCT has been reported for Ln and Ln doped Bi hybrid materials,^{28, 63} the heterometallic phases reported herein are uniquely capable of exhibiting emissive color tuning upon UV and visible excitation.

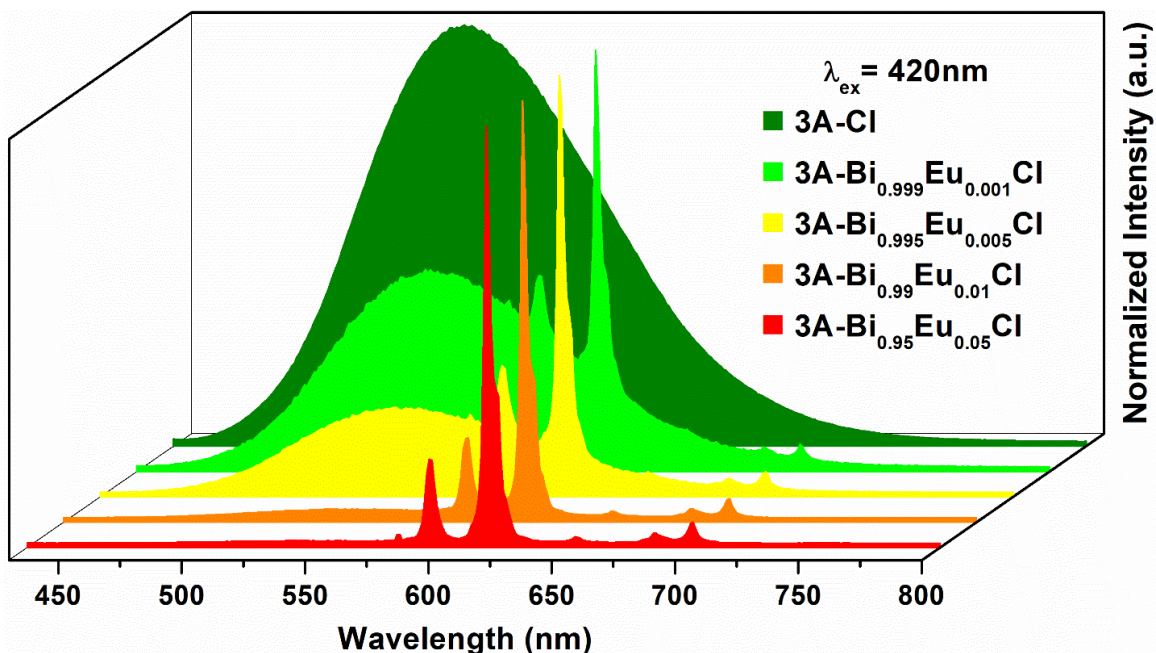


Figure 15: Normalized emission of $3A-Cl$, $3A-Bi_{0.999}Eu_{0.001}Cl$, $3A-Bi_{0.995}Eu_{0.005}Cl$, $3A-Bi_{0.99}Eu_{0.01}Cl$, and $3A-Bi_{0.95}Eu_{0.05}Cl$ upon common excitation at $\lambda_{ex} = 420$ nm.

The emission chromaticity and corresponding CIE coordinates for the luminescent compounds reported in this work are summarized in Figure 16. For the homometallic phases, the emission from the BiBr phases was inherently more yellow than the light green-yellow emissions of the BiCl phases. Trace doping of between 0.1-5% Eu relative to Bi synthetic loading yielded the heterometallic phases that exhibit yellow-green, yellow, light orange, orange, and red emission, with the color based on the relative contributions of the broad emission attributed to the ligand and the sharp transitions ascribed to Eu metal centered emission.

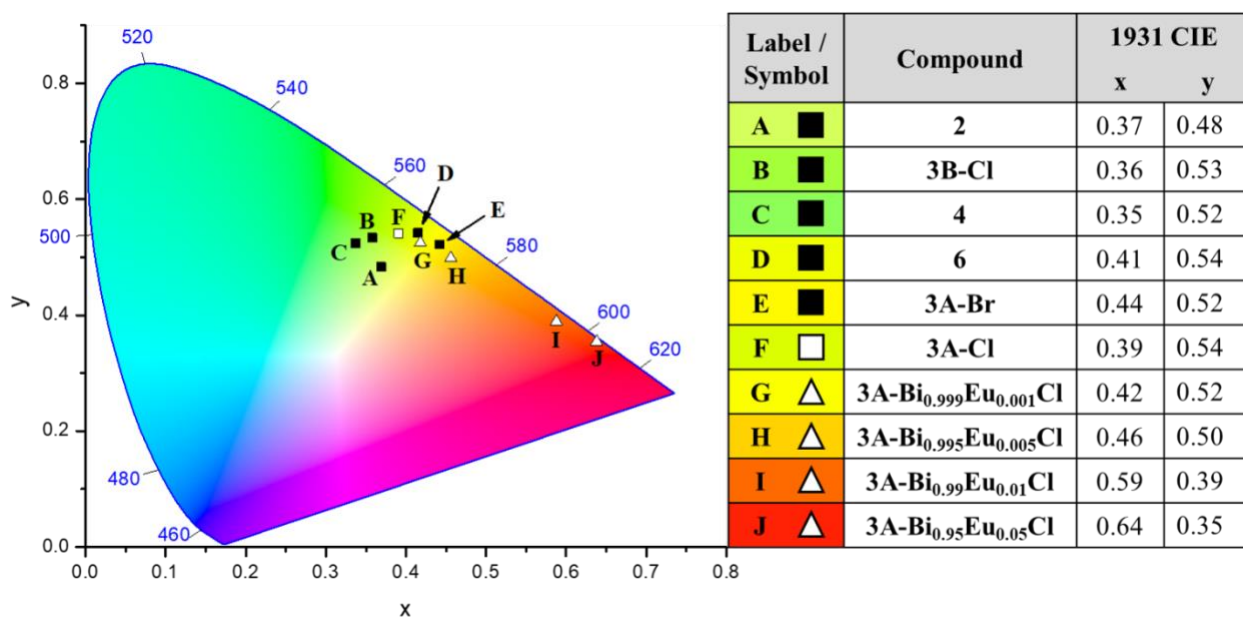


Figure 16: CIE chromaticity plot for the compounds reported in this work. Calculated coordinates for Bi homometallic phases **2**, **3A-Br**, **3B-Cl**, **4**, and **6** are rendered as black squares. Compound **3A-Cl** is shown as a white square and the Eu doped series, **3A-Bi_{0.999}Eu_{0.001}Cl**, **3A-Bi_{0.995}Eu_{0.005}Cl**, **3A-Bi_{0.99}Eu_{0.01}Cl**, and **3A-Bi_{0.95}Eu_{0.05}Cl**, is represented by white triangles.

Time dependent luminescent studies were performed to provide further insight into the nature and potential origins of the observed emissions. Lifetime measurements monitored at the principal $^5D_0 \rightarrow ^7F_2$ Eu emission ($\lambda_{Em} = 616$ nm) for the heterometallic phases **3A-Bi_{0.95}Eu_{0.05}Cl**, **3A-Bi_{0.99}Eu_{0.01}Cl**, and **3A-Bi_{0.995}Eu_{0.005}Cl**, revealed lifetimes of 1060(3), 1052(4), and 1041(3) μ s, respectively. These values are consistent with other emissive Eu species.⁶⁴ The decay spectra and corresponding exponential fits are displayed in Figures S37-S39. The region fitted for the lifetime calculations was set over 160-7000 μ s; however, a rapid initial decay between 110-150 μ s was observed. The relative influence of this initial decay was shown to increase with decreasing Eu composition and the corresponding increases in the relative influence of the aforementioned broad-band transition. Attempts to determine the lifetime of this initial decay could not be reliably evaluated due to instrumental limitations. Yet, the lifetime value is known to be less than 10 μ s, as

in the homometallic phases. Slight decreases in the lifetime of Eu emission with increasing influence of a second emissive feature suggest Eu emission and the broad LMXCT/ligand emission observed in the **3A-Bi_{1-x}Eu_xCl** ($x = 0.001, 0.005, 0.01, 0.05$) series are competitive radiative pathways. Nevertheless, the presence of these simultaneous emissions with relatively short- and long-lived lifetimes afford color tuning of the observed emission through applied delays in time resolved luminescence studies. As shown by the emission spectra of **3A-Bi_{0.999}Eu_{0.001}Cl** and **Bi_{0.995}Eu_{0.005}Cl** (Figures S40 and S41) the observed emission profile and corresponding chromaticity can be controlled by variation of applied delays in the timeframe of collection. Upon increases in the observation delay time between 0 to 50 μ s, influence of the broad feature centered at 550 nm is incrementally diminished; however, longer lived Eu emission is retained and subsequent red chromaticity is seen. While the discussed luminescent phenomena produced by these homo- and heterometallic Bi halide organic materials may be desirable, further insight into their structural origins is needed to fully understand, control, and optimize their potential application.

Structure-Property Relationships.

The Bi halide organic hybrid materials reported herein are built from a range of monomeric and dimeric complexes, and provide solid-state snapshots into bismuth-ligand coordination chemistry. Indeed, the solid-state complexes provide models from which the impact of ligand substitution on luminescent behavior may be understood. No appreciable luminescence was observed for compounds **1** and **5**. This is likely due, in part, to the incorporation of solvent water and methanol that are known to enable non-radiative decay via molecular vibrations.⁶⁵⁻⁶⁶ This assertion is supported by the observation of a previously reported luminescent Bi₂Cl₆(terpy)₂ phase,³³ upon

removal of water from **1** (Figure S19). Aggregation of organic and inorganic-organic complexes through intermolecular interactions in solution and the solid state has been shown to affect the luminescent behavior of these species by limiting molecular vibrations and the resultant non-radiative decay pathways.⁶⁷⁻⁶⁹ Therefore, the potential for supramolecular interactions to assist luminescent transitions should not be discounted. To this point, the extensive π - π stacking interactions of terpy and TC ligands observed within these phases are anticipated to serve a secondary but supportive role of increasing structural rigidity and minimizing luminescence quenching due to vibrational pathways.

As shown by the computational studies, the organic ligands used in this work and their associated orbitals were involved in the observed luminescent transitions. While the π^* orbitals of terpy serve as the principal virtual states for energy transfer and subsequent emission, the TC ligand orbitals contributed to many of the underlying occupied energy states and corresponding higher energy LLCT transitions. Yet the presence and associated energy state transitions of the BiX subunit are arguably the most significant factor with respect to the luminescent properties of the materials; energy transfer between the BiX subunit and ligand excited states underpins the luminescent behavior observed for **2**, **3A-Br**, **3B-Cl**, **4**, and **6**. The electronic structure calculations as well as the spectra obtained experimentally also show that ligand orientation and the number of halide substituents play an important role in the extension of the excitation bands into the visible region. Furthermore, the interplay of the Bi $6s^2$ stereochemical activity and ensuing distortion of the coordination sphere including elongation of Bi-X bond lengths may also lead to shifting of absorbance/excitation features given their attributed relevance to the HOMO energy state. For example, isostructural monomers **3A-Cl** and **3B-Cl** possess Bi-Cl distances of 2.5879(1) and 2.6228(1) Å, respectively. With this increase in bond length, a concurrent blue shift is observed in

the corresponding calculated absorption spectra (Figure S57), the experimental solid-state UV-Vis spectra (Figure S44), and the low energy excitation maxima (Figure 8). Additionally, isostructural models **6(c)** and **6(d)** exhibit Bi-Br distances of 2.8144(2) and 2.9757(2), respectively, and also demonstrate blue shifting of the calculated lowest energy transition as the Bi-X bond distance increases (Figure S55). This observation is consistent with other hybrid and inorganic systems,^{32, 70-73} wherein distortions in metal center coordination led to shifts in energy states and the corresponding transitions. Increased stereochemical activity of the Bi lone pair electrons is indicative of increased p orbital character and sp hybridization.^{32, 71} In the presented work, such hybridization as well as mixing with the halide p orbital contributions, may facilitate a lower energy HOMO than that observed for Bi compounds for which the lone pair is more stereochemically inert. Concurrent with the distortion of the Bi coordination environment, increased torsion of the terpy ligand away from its typical planar motif appears to increase the LUMO, as previously reported.⁶¹ The increased distortions of the metal-halide unit and terpy ligands result in a widening of the HOMO → LUMO transition and manifests as a blue shifting of absorption bands to higher energy.

The importance of the BiX sub-unit to the luminescent properties of the reported compounds is further evidenced in the **3A-Bi_{1-x}Eu_xCl** (x = 0.001, 0.005, 0.01, 0.05) series. This heterometallic series exhibited unprecedented dual emission from both Eu and LXMCT/ligand pathways upon UV and visible excitation. By comparison, the previously reported heterometallic Eu doped phase, Bi_{0.84}Eu_{0.16}(terpy)(k₂-TC)₃, lacked halide substituents and exhibited only Eu emission with no visible excitation pathway.⁵² The excitation and emission spectra for **3A-Cl** and **3A-Bi_{0.995}Eu_{0.005}Cl**, as well as previously reported BiEu- and Eu-terpy-TC reference compounds are illustrated in Figure S42.⁵¹⁻⁵² Comparison of these spectra highlights the departure from customary

UV excitation and subsequent Eu emission from phases absent halide substituents towards visible excitation and simultaneous emissions that originate, in part, from BiX-to-ligand transitions for the Bi-halide-terpy-TC complexes. Even though these simultaneous emissions likely result from competitive pathways, they also afford compositional PLCT as a function of Eu doping percentage. Variation of Ln doping percentages to achieve PLCT is a well-established design strategy in luminescent materials literature,⁷⁴⁻⁷⁵ yet to the best of our knowledge the Eu doped Bi-halide organic hybrid materials reported herein provide one of the first examples of emissive color tuning within hybrid materials that can be achieved upon visible excitation.

It is worth noting that similar XMLCT pathways serving as intermediate energy states have recently been observed in Bi- and Sb-halide materials.^{59, 76-77} Botta and colleagues, for example, reported several BiBr-dioxide pyridine coordination polymers that display mechanochromism, for which the excitation and emission are attributed to XMLCT and inverse LXMCT pathways, respectively.^{23, 31, 59} These energy transfer pathways were assigned primarily to higher energy absorption features ($\lambda = <350$ nm), yet visible excitation features are often present as well. These previously reported materials possess three or more Br ions per Bi metal center and excitation bands that extend well beyond 500 nm. These results are consistent with our findings in which mixed BiX orbital contributions are involved in the luminescent transitions of the reported materials as well as our experimentally and computationally derived trend that with increasing halide complexation, excitation extends further into the visible region. The relationship between the number of bound halides and shifting of the excitation wavelengths is also consistent with reports of red shifting in absorbance bands with increasing halide incorporation for perovskite precursor solutions/thin film species such as PbI_2 , $(\text{PbI}_3)^-$, $(\text{PbI}_4)^{2-}$, and potentially $(\text{Pb}_2\text{I}_9)^{5-}$.⁷⁸⁻⁸¹ This trend has also been observed for other main group metal halide species, including Bi.⁸² A

natural extension of this trend would correlate with the well-documented visible light absorbance/photovoltaic properties of main group metal perovskites, including Bi, that almost exclusively possess six halides bound to each metal center, and for which distortion of the metal coordination environment and halide identity directly impact the observed photoactive behavior.^{20,}
⁸³ While these observations may not be universal for all Bi halide materials, such correlations seem to be a promising avenue towards controlling excitation pathways and achieving tailored luminescent properties.

CONCLUSION

Seven novel bismuth(III) halide phases consisting of 2,2',6',2''-terpyridine and/or 2-thiophenemonocarboxylate ligands were isolated through systematic variation of synthetic conditions. The structures are built from monomeric and dimeric complexes that exhibit differences in the number of bound halide/TC units per metal ion as well supramolecular packing interactions. The homometallic phases **2**, **3A-Cl**, **3A-Br**, **3B-Cl**, **4**, **6** exhibited broad yellow/green emission. Notably, the emissions could be observed upon visible excitation ($\lambda_{\text{Ex}} = > 400 \text{ nm}$). Computational analysis based on DFT calculations and experimentally deduced structures were performed in an effort to better understand the origin of the visible excitation pathways. Analyses of frontier molecular orbital energies showed that the visible absorbance features could be attributed to intramolecular metal-halide to ligand charge transfer processes (XMLCT). Furthermore, the extension of the transitions deeper into the visible region was found to depend on the number and orientation of halide ions coordinated to the Bi metal center. This computationally derived trend was also apparent upon inspection of the solid-state structures and the experimental excitation spectra. Furthermore, the extent of Bi $6s^2$ stereochemical activity is

anticipated to influence the Bi-X bond distances and corresponding HOMO energies, while distortions of the terpy ligand impact the LUMO energies. Increased separation of these energy levels with increased distortion of the metal center and terpy ligand are reflected in the experimental and computational data as blue shifts in low energy absorption and excitation transitions. Therefore, these tailorable structural features are predicted to serve as a promising design features that may be harnessed towards controlling and tuning luminescent properties, such as visible excitation. Luminescent studies of a heterometallic series, **3A-Bi_{1-x}Eu_xCl** ($x = 0.001, 0.005, 0.01, 0.05$), revealed simultaneous ligand/LXMCT and Eu emissions whose relative intensities were tunable based on Eu composition. Subsequently, photoluminescent color tuning from green-yellow to red emission was achieved; increased Eu incorporation was found to increase the influence of Eu³⁺ emission on the overall emission chromaticity. Additionally, the highlighted visible excitation seen in the homometallic Bi phases was retained across the Eu doped heterometallic series. The lack of visible excitation in related Eu only and Eu doped Bi phases without halide substituents further suggests that the BiX sub-unit is crucial to obtaining this useful luminescent property. As demonstrated through the combined experimental and computational examination of structure property relationships reported herein, Bi halide organic materials present unique luminescent behaviors that warrant further exploration towards the design of materials with tailorable luminescent properties.

ASSOCIATED CONTENT

Supporting Information.

The Supporting Information is available free of charge on the ACS Publications website at DOI:

Synthetic details, combustion elemental analyses, crystallographic refinement details, thermal ellipsoid plots, powder X-ray diffraction patterns, excitation and emission spectra, time-resolved luminescence spectra, Raman spectra, and additional computational results.

Accession Codes.

CCDC 2063326-2063333 contain the supplementary crystallographic data for this paper. These data can be obtained free of charge via www.ccdc.cam.ac.uk/data_request/cif, or by emailing data_request@ccdc.cam.ac.uk, or by contacting The Cambridge Crystallographic Data Centre, 12 Union Road, Cambridge CB2 1EZ, UK; fax +44 1223 336033.

AUTHOR INFORMATION

Corresponding Authors.

* Karah E. Knope

kek44@georgetown.edu

Department of Chemistry, Georgetown University, 37th and O Streets, NW, Washington, D.C. 20057, USA

* Florent Réal

florent.real@univ-lille.fr

Univ. Lille, CNRS, UMR 8523–PhLAM–Physique des Lasers Atomes et Molécules, 59000 Lille, France

Author Contributions.

The manuscript was written through contributions of all authors. All authors have given approval to the final version of the manuscript.

Funding Sources.

The Clare Boothe Luce Program (KEK) and the DoD SMART Scholarship Program (RLA).

The Program “Investissement d’avenir” (LABEX CaPPA/ANR-11-LABX-0005-01 and I-SITE ULNE/ANR-16- IDEX-0004 ULNE).

Ministry of Higher Education and Research.

Hauts de France Council and European Regional Development Fund (ERDF) through the Contrat de Projets état-Région (CPER-CLIMIBIO).

Notes.

ORCID:

KEK: 0000-0002-5690-715X

RLA: 0000-0001-6141-5486

JAB: 0000-0002-3419-5163

FR: 0000-0002-5163-1545

VV: 0000-0002-2202-3858

ACKNOWLEDGMENT

The authors gratefully acknowledge the Clare Boothe Luce Foundation (KEK) and the DoD SMART Scholarship Program (RLA) for their support. FR and VV acknowledge support by the French Government through the Program “Investissement d’avenir” (LABEX CaPPA/ANR-11-LABX-0005-01 and I-SITE ULNE/ANR-16- IDEX-0004 ULNE), as well as by the Ministry of Higher Education and Research, Hauts de France Council and European Regional Development Fund (ERDF) through the Contrat de Projets état-Région (CPER-CLIMIBIO).

ABBREVIATIONS

PLCT, photoluminescent color tuning; WLE, white light emission, LED, light emitting diode; TCA, 2-thiophene monocarboxylic acid; TC, 2-thiophene monocarboxylate; terpy, 2,2',6',2''-terpyridine; CIE, Commission Internationale d'Eclairage; ILCT, Intra/interligand Charge Transfer; XMLCT, Halide-Metal to Ligand Charge Transfer; XLCT, Halide to Ligand Charge Transfer.

REFERENCES

1. Li, X.; Gao, X.; Zhang, X.; Shen, X.; Lu, M.; Wu, J.; Shi, Z.; Colvin, V. L.; Hu, J.; Bai, X.; Yu, W. W.; Zhang, Y., Lead-Free Halide Perovskites for Light Emission: Recent Advances and Perspectives. *Advanced Science* **2021**, *8* (4), 2003334.
2. Leng, M. Y.; Yang, Y.; Zeng, K.; Chen, Z. W.; Tan, Z. F.; Li, S. R.; Li, J. H.; Xu, B.; Li, D. B.; Hautzinger, M. P.; Fu, Y. P.; Zhai, T. Y.; Xu, L.; Niu, G. D.; Jin, S.; Tang, J., All-Inorganic Bismuth-Based Perovskite Quantum Dots with Bright Blue Photoluminescence and Excellent Stability. *Advanced Functional Materials* **2018**, *28* (1), 11.
3. Lin, Y.-C.; Karlsson, M.; Bettinelli, M., Inorganic Phosphor Materials for Lighting. *Topics in Current Chemistry* **2016**, *374* (2), 21.
4. Wei, Y.; Cheng, Z. Y.; Lin, J., An overview on enhancing the stability of lead halide perovskite quantum dots and their applications in phosphor-converted LEDs. *Chemical Society Reviews* **2019**, *48* (1), 310-350.
5. Li, X.; Gao, X.; Shi, W.; Ma, H., Design Strategies for Water-Soluble Small Molecular Chromogenic and Fluorogenic Probes. *Chemical Reviews* **2014**, *114* (1), 590-659.
6. Klymchenko, A. S., Solvatochromic and Fluorogenic Dyes as Environment-Sensitive Probes: Design and Biological Applications. *Accounts of Chemical Research* **2017**, *50* (2), 366-375.
7. Toma, O.; Mercier, N.; Botta, C., Process-dependent reversible mechanochromic luminescence of bismuth based polymorphs. *Journal of Materials Chemistry C* **2016**, *4* (25), 5940-5944.
8. Dalapati, R.; Nandi, S.; Van Hecke, K.; Biswas, S., Fluorescence Modulation of an Aggregation-Induced Emission Active Ligand via Rigidification in a Coordination Polymer and Its Application in Singlet Oxygen Sensing. *Crystal Growth & Design* **2019**, *19* (11), 6388-6397.
9. Yin, H.-Q.; Wang, X.-Y.; Yin, X.-B., Rotation Restricted Emission and Antenna Effect in Single Metal–Organic Frameworks. *Journal of the American Chemical Society* **2019**, *141* (38), 15166-15173.
10. Muller-Buschbaum, K.; Beuerle, F.; Feldmann, C., MOF based luminescence tuning and chemical/physical sensing. *Microporous and Mesoporous Materials* **2015**, *216*, 171-199.
11. Xia, Z.; Meijerink, A., Ce³⁺-Doped garnet phosphors: composition modification, luminescence properties and applications. *Chemical Society Reviews* **2017**, *46* (1), 275-299.

12. do Nascimento, J. F. S.; de Araujo, A. M. U.; Kulesza, J.; Monteiro, A. F. D.; Alves, S.; Barros, B. S., Solid-state tunable photoluminescence in gadolinium-organic frameworks: effects of the Eu³⁺ content and co-doping with Tb³⁺. *New Journal of Chemistry* **2018**, *42* (7), 5514-5522.
13. Akkerman, Q. A.; D'Innocenzo, V.; Accornero, S.; Scarpellini, A.; Petrozza, A.; Prato, M.; Manna, L., Tuning the Optical Properties of Cesium Lead Halide Perovskite Nanocrystals by Anion Exchange Reactions. *Journal of the American Chemical Society* **2015**, *137* (32), 10276-10281.
14. Zarick, H. F.; Soetan, N.; Erwin, W. R.; Bardhan, R., Mixed halide hybrid perovskites: a paradigm shift in photovoltaics. *Journal of Materials Chemistry A* **2018**, *6* (14), 5507-5537.
15. Hattori, Y.; Kusamoto, T.; Nishihara, H., Luminescence, Stability, and Proton Response of an Open-Shell (3,5-Dichloro-4-pyridyl)bis(2,4,6-trichlorophenyl)methyl Radical. *Angewandte Chemie* **2014**, *126* (44), 12039-12042.
16. Peng, Q.; Obolda, A.; Zhang, M.; Li, F., Organic Light-Emitting Diodes Using a Neutral π Radical as Emitter: The Emission from a Doublet. *Angewandte Chemie* **2015**, *127* (24), 7197-7201.
17. D'Aléo, A.; Picot, A.; Beeby, A.; Gareth Williams, J. A.; Le Guennic, B.; Andraud, C.; Maury, O., Efficient Sensitization of Europium, Ytterbium, and Neodymium Functionalized Tris-Dipicolinate Lanthanide Complexes through Tunable Charge-Transfer Excited States. *Inorganic Chemistry* **2008**, *47* (22), 10258-10268.
18. Armelao, L.; Quici, S.; Barigelletti, F.; Accorsi, G.; Bottaro, G.; Cavazzini, M.; Tondello, E., Design of luminescent lanthanide complexes: From molecules to highly efficient photo-emitting materials. *Coordination Chemistry Reviews* **2010**, *254* (5-6), 487-505.
19. Hasegawa, Y.; Nakagawa, T.; Kawai, T., Recent progress of luminescent metal complexes with photochromic units. *Coordination Chemistry Reviews* **2010**, *254* (21), 2643-2651.
20. Jin, Z.; Zhang, Z.; Xiu, J.; Song, H.; Gatti, T.; He, Z., A critical review on bismuth and antimony halide based perovskites and their derivatives for photovoltaic applications: recent advances and challenges. *Journal of Materials Chemistry A* **2020**, *8* (32), 16166-16188.
21. Meng, X.; Zhang, Z., Bismuth-based photocatalytic semiconductors: Introduction, challenges and possible approaches. *Journal of Molecular Catalysis A: Chemical* **2016**, *423*, 533-549.
22. Shen, N.; Wang, Z.; Jin, J.; Gong, L.; Zhang, Z.; Huang, X., Phase transitions and photoluminescence switching in hybrid antimony(iii) and bismuth(iii) halides. *CrystEngComm* **2020**, *22* (20), 3395-3405.
23. Toma, O.; Allain, M.; Meinardi, F.; Forni, A.; Botta, C.; Mercier, N., Bismuth-Based Coordination Polymers with Efficient Aggregation-Induced Phosphorescence and Reversible Mechanochromic Luminescence. *Angewandte Chemie-International Edition* **2016**, *55* (28), 7998-8002.
24. Heine, J.; Wehner, T.; Bertermann, R.; Steffen, A.; Müller-Buschbaum, K., 2∞ [Bi₂Cl₆(pyz)₄]: A 2D-Pyrazine Coordination Polymer As Soft Host Lattice for the Luminescence of the Lanthanide Ions Sm³⁺, Eu³⁺, Tb³⁺, and Dy³⁺. *Inorganic Chemistry* **2014**, *53* (14), 7197-7203.
25. Smith, M. D.; Karunadasa, H. I., White-Light Emission from Layered Halide Perovskites. *Accounts of Chemical Research* **2018**, *51* (3), 619-627.

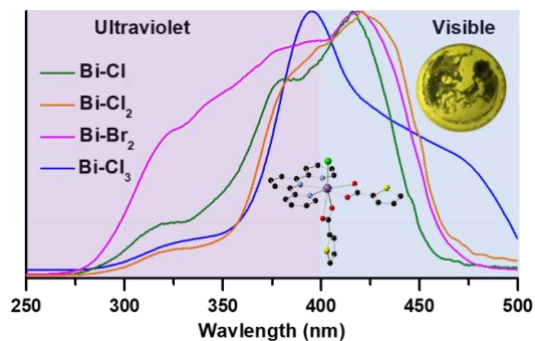
26. Rhauderwiek, T.; dos Santos Cunha, C.; Terraschke, H.; Stock, N., Bismuth Coordination Polymers with 2,4,6-Pyridine Tricarboxylic Acid: High-Throughput Investigations, Crystal Structures and Luminescence Properties. *European Journal of Inorganic Chemistry* **2018**, *2018* (27), 3232-3240.
27. Zhang, X. P.; Wang, D. G.; Su, Y.; Tian, H. R.; Lin, J. J.; Fenga, Y. L.; Cheng, J. W., Luminescent 2D bismuth-cadmium-organic frameworks with tunable and white light emission by doping different lanthanide ions. *Dalton Transactions* **2013**, *42* (29), 10384-10387.
28. Cunha, C. S.; Köppen, M.; Terraschke, H.; Friedrichs, G.; Malta, O. L.; Stock, N.; Brito, H. F., Luminescence tuning and single-phase white light emitters based on rare earth ions doped into a bismuth coordination network. *Journal of Materials Chemistry C* **2018**, *6* (46), 12668-12678.
29. Deibert, B. J.; Velasco, E.; Liu, W.; Teat, S. J.; Lustig, W. P.; Li, J., High-Performance Blue-Excitable Yellow Phosphor Obtained from an Activated Solvochromic Bismuth-Fluorophore Metal–Organic Framework. *Crystal Growth & Design* **2016**, *16* (8), 4178-4182.
30. Sorg, J. R.; Wehner, T.; Matthes, P.; Sure, R.; Grimme, S.; Heine, J.; Müller-Buschbaum, K., Bismuth as Versatile Cation for Luminescence in Coordination Polymers from BiX_{3/4},4'-bipy: Understanding of Photophysics by Quantum Chemical Calculations and Structural Parallels to Lanthanides. *Dalton Transactions* **2018**, *47* (23), 7669-7681.
31. Toma, O.; Mercier, N.; Botta, C., N-Methyl-4,4'-bipyridinium and N-Methyl-N'-oxide-4,4'-bipyridinium Bismuth Complexes – Photochromism and Photoluminescence in the Solid State. *European Journal of Inorganic Chemistry* **2013**, *2013* (7), 1113-1117.
32. Sorg, J. R.; Schneider, T.; Wohlfarth, L.; Schäfer, T. C.; Sedykh, A.; Müller-Buschbaum, K., Sb- and Bi-based coordination polymers with N-donor ligands with and without lone-pair effects and their photoluminescence properties. *Dalton Transactions* **2020**, *49* (15), 4904-4913.
33. Adcock, A. K.; Ayscue, R. L.; Breuer, L. M.; Verwiel, C. P.; Marwitz, A. C.; Bertke, J. A.; Vallet, V.; Réal, F.; Knope, K. E., Synthesis and photoluminescence of three bismuth(iii)-organic compounds bearing heterocyclic N-donor ligands. *Dalton Transactions* **2020**, *49* (33), 11756-11771.
34. APEX3, SADABS, SAINT, SHELXTL, XCIF, XPREP. *Bruker AXS Inc.* **2016**, *Madison, WI, USA*.
35. Hubschle, C. B.; Sheldrick, G. M.; Dittrich, B., ShelXle: a Qt graphical user interface for SHELXL. *Journal of Applied Crystallography* **2011**, *44* (6), 1281-1284.
36. Sheldrick, G., Crystal structure refinement with SHELXL. *Acta Crystallographica Section C* **2015**, *71* (1), 3-8.
37. Spek, A., Single-crystal structure validation with the program PLATON. *Journal of Applied Crystallography* **2003**, *36* (1), 7-13.
38. Neese, F., The ORCA program system. *Wiley Interdiscip. Rev.: Comput. Mol. Sci.* **2012**, *2*, 73-78.
39. Neese, F., Software update: the ORCA program system, version 4.0. *Wiley Interdiscip. Rev.: Comput. Mol. Sci.* **2017**, *8* (1), e1327.
40. Yanai, T.; Tew, D. P.; Handy, N. C., A new hybrid exchange-correlation functional using the Coulomb-attenuating method (CAM-B3LYP). *Chem. Phys. Lett* **2004**, *393*, 51-57.
41. Weigend, F.; Ahlrichs, R., Balanced basis sets of split valence, triple zeta valence and quadruple zeta valence quality for H to Rn: Design and assessment of accuracy. *Physical Chemistry Chemical Physics* **2005**, *7* (18), 3297-3305.

42. Metz, B.; Stoll, H.; Dolg, M., Small-core multiconfiguration-Dirac–Hartree–Fock-adjusted pseudopotentials for post-d main group elements: Application to PbH and PbO. *The Journal of Chemical Physics* **2000**, *113* (7), 2563-2569.
43. Bannwarth, C.; Grimme, S., A simplified time-dependent density functional theory approach for electronic ultraviolet and circular dichroism spectra of very large molecules. *Comput. Theor. Chem.* **2014**, *1040*, 45-53.
44. Grimme, S., A simplified Tamm-Dancoff density functional approach for the electronic excitation spectra of very large molecules. *The Journal of Chemical Physics* **2013**, *138* (24), 244104.
45. Risthaus, T.; Hansen, A.; Grimme, S., Excited states using the simplified Tamm–Dancoff-Approach for range-separated hybrid density functionals: development and application. *Physical Chemistry Chemical Physics* **2014**, *16* (28), 14408-14419.
46. Neese, F.; Wennmohs, F.; Hansen, A.; Becker, U., Efficient, approximate and parallel Hartree–Fock and hybrid DFT calculations. A ‘chain-of-spheres’ algorithm for the Hartree–Fock exchange. *Chemical Physics* **2009**, *356* (1), 98-109.
47. Petrenko, T.; Kossmann, S.; Neese, F., Efficient time-dependent density functional theory approximations for hybrid density functionals: Analytical gradients and parallelization. *The Journal of Chemical Physics* **2011**, *134* (5), 054116.
48. Salonen, L. M.; Ellermann, M.; Diederich, F., Aromatic Rings in Chemical and Biological Recognition: Energetics and Structures. *Angewandte Chemie International Edition* **2011**, *50* (21), 4808-4842.
49. Robin, A. Y.; Fromm, K. M., Coordination polymer networks with O- and N-donors: What they are, why and how they are made. *Coordination Chemistry Reviews* **2006**, *250* (15), 2127-2157.
50. Janiak, C., A critical account on π – π stacking in metal complexes with aromatic nitrogen-containing ligands. *Journal of the Chemical Society, Dalton Transactions* **2000**, (21), 3885-3896.
51. Batrice, R. J.; Ridenour, J. A.; Ayscue, R. L.; Bertke, J. A.; Knope, K. E., Synthesis, structure, and photoluminescent behaviour of molecular lanthanide-2-thiophenecarboxylate-2,2':6',2''-terpyridine materials. *Crystengcomm* **2017**, *19* (35), 5300-5312.
52. Batrice, R. J.; Ayscue, R. L.; Adcock, A. K.; Sullivan, B. R.; Han, S. Y.; Piccoli, P. M.; Bertke, J. A.; Knope, K. E., Photoluminescence of Visible and NIR-Emitting Lanthanide-Doped Bismuth-Organic Materials. *Chemistry-a European Journal* **2018**, *24* (21), 5630-5636.
53. Wei, Z.; Gu, Z.-Y.; Arvapally, R. K.; Chen, Y.-P.; McDougald, R. N.; Ivy, J. F.; Yakovenko, A. A.; Feng, D.; Omary, M. A.; Zhou, H.-C., Rigidifying Fluorescent Linkers by Metal–Organic Framework Formation for Fluorescence Blue Shift and Quantum Yield Enhancement. *Journal of the American Chemical Society* **2014**, *136* (23), 8269-8276.
54. Sutter-Fella, C. M.; Li, Y.; Amani, M.; Ager, J. W.; Toma, F. M.; Yablonovitch, E.; Sharp, I. D.; Javey, A., High Photoluminescence Quantum Yield in Band Gap Tunable Bromide Containing Mixed Halide Perovskites. *Nano Letters* **2016**, *16* (1), 800-806.
55. Al-Rasbi, N. K.; Sabatini, C.; Barigelletti, F.; Ward, M. D., Red-shifted luminescence from naphthalene-containing ligands due to π -stacking in self-assembled coordination cages. *Dalton Transactions* **2006**, (40), 4769-4772.
56. Adcock, A. K.; Gibbons, B.; Einkauf, J. D.; Bertke, J. A.; Rubinson, J. F.; de Lill, D. T.; Knope, K. E., Bismuth(III)-thiophenedicarboxylates as host frameworks for lanthanide ions:

- synthesis, structural characterization, and photoluminescent behavior. *Dalton Transactions* **2018**, 47 (38), 13419-13433.
57. Gomez, G. E.; D'Vries, R. F.; Lionello, D. F.; Aguirre-Diaz, L. M.; Spinosa, M.; Costa, C. S.; Fuertes, M. C.; Pizarro, R. A.; Kaczmarek, A. M.; Ellena, J.; Rozes, L.; Iglesias, M.; Van Deun, R.; Sanchez, C.; Monge, M. A.; Soler-Illia, G., Exploring physical and chemical properties in new multifunctional indium-, bismuth-, and zinc-based 1D and 2D coordination polymers. *Dalton Transactions* **2018**, 47 (6), 1808-1818.
58. Bu, Q.; Wang, G.-E.; Xu, G.; Long, X.; Xia, Y., Luminescent inorganic–organic hybrid with tunable red light emissions by neutral molecule modification. *Inorganic Chemistry Communications* **2020**, 116, 107909.
59. Toma, O.; Mercier, N.; Allain, M.; Meinardi, F.; Forni, A.; Botta, C., Mechanochromic Luminescence of N,N'-Dioxide-4,4'-bipyridine Bismuth Coordination Polymers. *Crystal Growth & Design* **2020**, 20 (12), 7658-7666.
60. Wang, G.; Sun, Q.; Liu, Y.; Huang, B.; Dai, Y.; Zhang, X.; Qin, X., A Bismuth-Based Metal–Organic Framework as an Efficient Visible-Light-Driven Photocatalyst. *Chemistry – A European Journal* **2015**, 21 (6), 2364-2367.
61. Nocton, G.; Booth, C. H.; Maron, L.; Andersen, R. A., Influence of the Torsion Angle in 3,3'-Dimethyl-2,2'-bipyridine on the Intermediate Valence of Yb in (C₅Me₅)₂Yb(3,3'-Me₂-bipy). *Organometallics* **2013**, 32 (19), 5305-5312.
62. Bünzli, J. C. G., On the design of highly luminescent lanthanide complexes. *Coordination Chemistry Reviews* **2015**, 293, 19-47.
63. Meyer, L. V.; Schonfeld, F.; Müller-Buschbaum, K., Lanthanide based tuning of luminescence in MOFs and dense frameworks - from mono- and multimetal systems to sensors and films. *Chemical Communications* **2014**, 50 (60), 8093-8108.
64. Bünzli, J.-C. G.; Chauvin, A.-S.; Kim, H. K.; Deiters, E.; Eliseeva, S. V., Lanthanide luminescence efficiency in eight- and nine-coordinate complexes: Role of the radiative lifetime. *Coordination Chemistry Reviews* **2010**, 254 (21), 2623-2633.
65. Beeby, A.; Clarkson, I. M.; Dickins, R. S.; Faulkner, S.; Parker, D.; Royle, L.; de Sousa, A. S.; Williams, J. A. G.; Woods, M., Non-radiative deactivation of the excited states of europium, terbium and ytterbium complexes by proximate energy-matched OH, NH and CH oscillators: an improved luminescence method for establishing solution hydration states. *Journal of the Chemical Society-Perkin Transactions 2* **1999**, (3), 493-503.
66. Maillard, J.; Klehs, K.; Rumble, C.; Vauthey, E.; Heilemann, M.; Fürstenberg, A., Universal quenching of common fluorescent probes by water and alcohols. *Chemical Science* **2021**, 12 (4), 1352-1362.
67. Hong, Y. N.; Lam, J. W. Y.; Tang, B. Z., Aggregation-induced emission: phenomenon, mechanism and applications. *Chemical Communications* **2009**, (29), 4332-4353.
68. Ostrowska, K.; Ceresoli, D.; Stadnicka, K.; Gryl, M.; Cazzaniga, M.; Soave, R.; Musielak, B.; Witek, Ł. J.; Goszczycki, P.; Grolik, J.; Turek, A. M., π - π -Induced aggregation and single-crystal fluorescence anisotropy of 5,6,10b-tri-aza-acephenanthrylene. *IUCrJ* **2018**, 5 (Pt 3), 335-347.
69. Du, X.; Fan, R. Q.; Wang, X. M.; Qiang, L. S.; Wang, P.; Gao, S.; Zhang, H. J.; Yang, Y. L.; Wang, Y. L., Combined Effect of Hydrogen Bonding and π center dot center dot center dot π Stacking Interactions in the Assembly of Indium(III) Metal-Organic Materials: Structure-Directing and Aggregation-Induced Emission Behavior. *Crystal Growth & Design* **2015**, 15 (5), 2402-2412.

70. Wheeler, R. A.; Kumar, P., Stereochemically Active or Inactive Lone Pair Electrons in Some 6-Coordinate, Group-15 Halides. *Journal of the American Chemical Society* **1992**, *114* (12), 4776-4784.
71. Vogler, A.; Nikol, H., The Structures of s_2 Metal Complexes in the Ground and sp Excited States. *Comments on Inorganic Chemistry* **1993**, *14* (4), 245-261.
72. Biswas, A.; Bakthavatsalam, R.; Mali, B. P.; Bahadur, V.; Biswas, C.; Raavi, S. S. K.; Gonnade, R. G.; Kundu, J., The metal halide structure and the extent of distortion control the photo-physical properties of luminescent zero dimensional organic-antimony(III) halide hybrids. *Journal of Materials Chemistry C* **2021**, *9* (1), 348-358.
73. Smith, M. D.; Jaffe, A.; Dohner, E. R.; Lindenberg, A. M.; Karunadasa, H. I., Structural origins of broadband emission from layered Pb–Br hybrid perovskites. *Chemical Science* **2017**, *8* (6), 4497-4504.
74. Wang, J.; Suffren, Y.; Daiguebonne, C.; Freslon, S.; Bernot, K.; Calvez, G.; Le Pollès, L.; Roiland, C.; Guillou, O., Multi-Emissive Lanthanide-Based Coordination Polymers for Potential Application as Luminescent Bar-Codes. *Inorganic Chemistry* **2019**, *58* (4), 2659-2668.
75. Zheng, Z.; Lu, H.; Wang, Y.; Bao, H.; Li, Z.-J.; Xiao, G.-P.; Lin, J.; Qian, Y.; Wang, J.-Q., Tuning of the Network Dimensionality and Photoluminescent Properties in Homo- and Heteroleptic Lanthanide Coordination Polymers. *Inorganic Chemistry* **2021**, *60* (3), 1359-1366.
76. Nicholas, A. D.; Halli, R. N.; Garman, L. C.; Cahill, C. L., Low-Dimensional Hybrid Indium/Antimony Halide Perovskites: Supramolecular Assembly and Electronic Properties. *The Journal of Physical Chemistry C* **2020**, *124* (47), 25686-25700.
77. Egger, D. A., Intermediate Bands in Zero-Dimensional Antimony Halide Perovskites. *The Journal of Physical Chemistry Letters* **2018**, *9* (16), 4652-4656.
78. Horváth, O.; Mikó, I., Spectra, equilibrium and photoredox chemistry of tri- and tetraiodoplumbate(II) complexes in acetonitrile. *Journal of Photochemistry and Photobiology A: Chemistry* **1998**, *114* (2), 95-101.
79. Stampelcoskie, K. G.; Manser, J. S.; Kamat, P. V., Dual nature of the excited state in organic–inorganic lead halide perovskites. *Energy & Environmental Science* **2015**, *8* (1), 208-215.
80. Stewart, R. J.; Grieco, C.; Larsen, A. V.; Doucette, G. S.; Asbury, J. B., Molecular Origins of Defects in Organohalide Perovskites and Their Influence on Charge Carrier Dynamics. *The Journal of Physical Chemistry C* **2016**, *120* (23), 12392-12402.
81. Kim, J.; Park, B.-w.; Baek, J.; Yun, J. S.; Kwon, H.-W.; Seidel, J.; Min, H.; Coelho, S.; Lim, S.; Huang, S.; Gaus, K.; Green, M. A.; Shin, T. J.; Ho-baillie, A. W. Y.; Kim, M. G.; Seok, S. I., Unveiling the Relationship between the Perovskite Precursor Solution and the Resulting Device Performance. *Journal of the American Chemical Society* **2020**, *142* (13), 6251-6260.
82. Oldenburg, K.; Vogler, A., Electronic Spectra and Photochemistry of Tin(II), Lead(II), Antimony(III), and Bismuth(III) Bromide Complexes in Solution. *Zeitschrift für Naturforschung B* **1993**, *48* (11), 1519-1523.
83. Jena, A. K.; Kulkarni, A.; Miyasaka, T., Halide Perovskite Photovoltaics: Background, Status, and Future Prospects. *Chemical Reviews* **2019**, *119* (5), 3036-3103.

FOR TABLE OF CONTENTS ONLY



The synthesis, structural characterization, and photoluminescent properties of a series of Bi-halide-organic hybrid compounds. A heterometallic lanthanide doped series displayed simultaneous emissive features and compositional based photoluminescent color tuning (PLCT). All emissive homo- and heterometallic phases exhibit visible excitation pathways that based on theoretical quantum mechanical calculations are attributed to halide-metal to ligand charge transfer (XMLCT).